# MAP7-driven cytoskeletal remodeling establishes epithelial polarity for male germ cell progression

Koji Kikuchi[1,7,8*], Toshihiko Fujimori[2], Mami Nakagawa[2], Keisuke Ohta[3], Ryuki Shimada[1], Sayoko Fujimura[4], Kei-ichiro Yasunaga[4], Shingo Usuki[4], Naoki Tani[4], Akira Nakamura[5], Kimi Araki[6], and Kei-ichiro Ishiguro[1,7,8]

[1]Department of Chromosome Biology, Institute of Molecular Embryology and Genetics, Kumamoto University, 2-2-1 Honjo, Chuo-ku, Kumamoto 860-0811, Japan

[2]Division of Embryology, National Institute for Basic Biology, 5-1 Higashiyama, Myodaiji, Okazaki, Aichi 444-8787, Japan

[3]Advanced Imaging Research Center, Kurume University School of Medicine, 67 Asahimachi, Kurume, Fukuoka 830-0011, Japan.

[4]Liaison Laboratory Research Promotion Center, Institute of Molecular Embryology and Genetics, Kumamoto University, 2-2-1 Honjo, Chuo-ku, Kumamoto 860-0811, Japan

[5]Department of Germline Development, Institute of Molecular Embryology and Genetics, Kumamoto University, 2-2-1 Honjo, Chuo-ku, Kumamoto 860-0811, Japan

[6]Institute of Resource Development and Analysis, Kumamoto University, 2-2-1 Honjo, Chuo-ku, Kumamoto 860-0811, Japan

Present address:

[7]Division of Comparative Pathophysiology, Next Generation In Vivo Research Exploratory Center (cNIVR), Chiba University, 1-8-1 Inohana, Chuo-ku, Chiba 260-8670, Japan

[8]Department of Biomedical Science, Graduate School of Medicine, Chiba University, 1-8-1 Inohana, Chuo-ku, Chiba 260-8670, Japan

***Corresponding author**: kojik@chiba-u.jp (K.K.)

**Abstract**

Sertoli cells establish a specialized apical domain essential for organizing the seminiferous epithelium and supporting germ cell development, yet the underlying mechanisms remain poorly understood. We identify MAP7 as a key regulator of cytoskeletal integration required for apical domain formation. MAP7 localizes to apical microtubules without overlapping stable, acetylated tubulin. MAP7 loss disrupts apical architecture, causes ectopic tight junction expansion, and prevents lumen formation during the first wave of spermatogenesis. Although microtubule stability is largely preserved in *Map7*-deficient Sertoli cells, their orientation is severely disrupted, indicating that MAP7 directs dynamic remodeling for proper apical organization. Proteomics shows that MAP7 associates with MYH9 and MYH10, and MYH9, normally enriched at luminal regions where microtubules and F-actin converge, becomes diffuse by *Map7* knockout, suggesting that MAP7 mediates spatial coupling of microtubules and actomyosin. Single-cell RNA sequencing shows that Sertoli cell differentiation largely persists without MAP7, whereas germ cells exhibit delayed meiotic progression with expanded pachytene subtypes. These findings position MAP7 as a cytoskeletal integrator linking epithelial polarity to germ cell progression, highlighting how tissue organization underlies fertility.

(175 words)

## Introduction

Sertoli cells are highly specialized epithelial cells that form the architectural scaffold of the seminiferous epithelium and orchestrate spermatogenesis. Unlike classical columnar epithelia, they undergo a unique form of polarization during postnatal development, culminating in the establishment of a distinct apical domain. This domain is critical for organizing the three-dimensional structure of the seminiferous tubules and creating a dynamic microenvironment that supports germ cell differentiation. As germ cells migrate from the basal to the luminal compartment, the Sertoli cell apical domain provides structural support and facilitates the localized delivery of trophic factors, adhesive interactions, and signaling cues necessary for maturation (O'Donnell et al. 2022). Disruption of apical architecture impairs germ cell development and leads to male infertility, underscoring the physiological importance of Sertoli cell polarity (Tanwar et al. 2012; Xiong et al. 2018; Heinrich et al. 2020; Heinrich et al. 2021). Despite its significance, the timing and molecular mechanisms driving Sertoli cell polarization and apical domain formation remain poorly understood.

Sertoli cell polarity is established and maintained through dynamic cytoskeletal remodeling (Dunleavy et al. 2019). Actin filaments, key components of ectoplasmic specializations (ES), play a central role in cell–cell adhesion and junctional integrity both among Sertoli cells and between Sertoli and germ cells (Grove and Vogl 1989; Byers et al. 1991). Basal ES includes actin-based adherens, and tight and gap junctions that contribute to the blood–testis barrier (BTB) and enable intercellular communication. Apical ES supports Sertoli–spermatid interactions critical for adhesion and maturation. Deletion of Sertoli-specific small GTPases, such as RAC1 and CDC42, which are key actin cytoskeleton regulators, disrupts apical ES formation and Sertoli cell polarity, resulting in defective spermatid differentiation and male infertility (Heinrich et al. 2020; Heinrich et al. 2021). Moreover, the role of the microtubule cytoskeleton in Sertoli cell polarization remains underexplored. Microtubules form bundles along the apical–basal axis and have been proposed to mediate intracellular transport and structural organization. Perturbations of microtubule organization, such as Sertoli cell-specific overexpression of the microtubule-nucleating protein γ-tubulin (Fleming et al. 2003b; Fleming et al. 2003a) or expression of a dominant-negative form of the microtubule plus-end tracking protein EB1 (Wang et al. 2008) , results in spermatogenic failure. Similarly, loss of the microtubule-severing enzyme KATNAL1 results in disorganized microtubules and premature release of elongating spermatids (Smith et al. 2012). Together, these findings highlight an essential yet poorly understood role of microtubule remodeling in Sertoli cell polarity and germ cell differentiation, particularly during the establishment of

epithelial polarity when the dynamics and regulation of microtubule remodeling remain largely unexplored.

Microtubule dynamics are tightly regulated by a variety of microtubule-associated proteins (MAPs) (Roll-Mecak 2020; Cleary and Hancock 2021). Among these, the MAP7 family has emerged as a key regulator of microtubules in cultured cells and in *Drosophila*. This family comprises four paralogs, namely MAP7, MAP7D1, MAP7D2, and MAP7D3, each containing an N-terminal microtubule-binding domain and a C-terminal kinesin-1–binding domain. These domains allow MAP7 proteins to stabilize microtubules and promote kinesin-1 loading, thereby facilitating intracellular transport (Sung et al. 2008; Metzger et al. 2012; Barlan et al. 2013; Kikuchi et al. 2018; Tymanskyj et al. 2018; Hooikaas et al. 2019; Pan et al. 2019; Kikuchi et al. 2022; Adler et al. 2024). MAP7 competes with other MAPs for microtubule binding, modulating motor protein distribution and activity in neurons (Monroy et al. 2018; Monroy et al. 2020). In HeLa cells, MAP7 and MAP7D1 cooperatively direct microtubule plus-ends to the cell cortex during migration and adhesion, independent of their roles in microtubule stabilization and growth (Kikuchi et al. 2018). In mice, MAP7 is expressed in both Sertoli and germ cells (Fabre-Jonca et al. 1998; Komada et al. 2000). Consistent with this, *Map7* gene-trap mutant mice exhibit reduced microtubule bundle formation in Sertoli cells and structural defects in spermatid manchettes, suggesting that MAP7 is critical for proper microtubule organization (Komada et al. 2000). However, it remains unclear whether MAP7 regulates dynamic microtubule remodeling during Sertoli cell polarization and contributes to germ cell development.

Microtubule remodeling plays an essential but poorly understood role in establishing Sertoli cell polarity and supporting germ cell differentiation. In this study, we aimed to elucidate the molecular mechanisms underlying apical domain formation in Sertoli cells during the first wave of spermatogenesis. We identified the microtubule-associated protein MAP7 as a central regulator of this process. MAP7 localizes to apical microtubules and promotes their dynamic remodeling, enabling spatial organization of cytoskeletal components essential for Sertoli cell polarity. Mechanistically, MAP7 forms a complex with non-muscle myosin II (NMII) heavy chains, MYH9 and MYH10, and directs MYH9 enrichment to luminal regions where microtubules and F-actin co-localize. In the absence of MAP7, MYH9 fails to accumulate apically and shows diffuse distribution, suggesting that MAP7-mediated integration of microtubule and actomyosin networks is essential for localized cytoskeletal remodeling. Although single-cell RNA sequencing (scRNA-Seq) reveals that Sertoli cell differentiation programs are largely maintained in the absence of MAP7, their transcriptional trajectories are

nevertheless perturbed. In contrast, *Map7*-deficient testes exhibit delayed germ cell development, characterized by an expansion of pachytene subpopulations. Together, these findings establish MAP7 as a key coordinator of cytoskeletal cross-talk, essential for apical domain formation and timely meiotic progression, thereby linking epithelial polarity to spermatogenesis.

## Results

### Localization pattern of MAP7 in Sertoli cells

*Map7* is expressed at the mRNA level in both Sertoli and male germ cells (Fabre-Jonca et al. 1998; Komada et al. 2000) ; however, its protein expression and subcellular localization remain uncharacterized. To address this, we generated *Map7-egfp* knock-in (*Map7-egfp*$^{KI}$) mic (Supplemental Fig. 1A, B). To ensure EGFP tagging did not disrupt MAP7 function, we confirmed homozygous viability and examined MAP7-EGFP$^{KI}$ localization in the fallopian tubes, where MAP7 expression had previously been analyzed using antibodies and *in vivo* electroporation of MAP7-EGFP (Kikuchi et al. 2018). Homozygous *Map7-egfp*$^{KI}$ mice were viable and fertile (Supplemental Fig. 1C). Consistent with prior observations, MAP7-EGFP$^{KI}$ localized along the planar axis of multiciliated cells on the ovarian (proximal) side of the fallopian tubes (Supplemental Fig. 1D), indicating that EGFP tagging does not interfere with MAP7 function *in vivo*.

We next examined MAP7-EGFP$^{KI}$ localization in adult testes by co-staining with TUBB3, a Sertoli cell-specific β-tubulin isoform. MAP7-EGFP$^{KI}$ colocalized with Sertoli microtubules labeled by TUBB3 (Fig. 1A, top) and exhibited a polarized distribution toward the luminal side (Fig. 1A, top), suggesting a role in microtubule dynamics. Additionally, MAP7-EGFP$^{KI}$ was expressed in step 9–11 spermatids, corresponding to phenotypes observed in *Map7* gene-trap mice (Fig. 1A, bottom), and colocalized with acetylated tubulin, a marker of manchette microtubule (Fig. 1B, bottom). Notably, MAP7-EGFP$^{KI}$ did not colocalize with long-lived stable microtubules outside the manchette (Fig. 1B, top). These localization patterns were further validated using an anti-MAP7 antibody (Fig. 1C). These findings demonstrate that MAP7 specifically localizes to apical microtubules in Sertoli cells and to manchette microtubules in step 9–11 spermatids, underscoring its potential role in microtubule dynamics during spermatogenesis.

### MAP7 is essential for the establishment of Sertoli cell polarity and apical domain formation

MAP7 localization in Sertoli cells, along with phenotypes observed in *Map7* gene-trap mice, suggests that MAP7 plays a role in establishing Sertoli cell polarity. However, prior studies used *Map7* gene-trap mice on a mixed B6.129 background, and complete loss of MAP7 protein was not validated (Komada et al. 2000). To directly assess the role of MAP7 in Sertoli cell polarity, we generated *Map7* knockout (KO) mice on a pure C57BL/6 background (Supplemental Fig. 2A–C). Complete loss of MAP7 protein in homozygous *Map7*$^{-/-}$ mice was

confirmed using two independent antibodies (Supplemental Fig. 2D). Consistent with observations in *Map7* gene-trap mice, *Map7*$^{-/-}$ males exhibited reduced testis size and spermatogenic defects (Supplemental Fig. 2E, F). Notably, the cauda epididymis of *Map7*$^{-/-}$ males contained no mature spermatozoa (Supplemental Fig. 2F), indicating male infertility. Heterozygous *Map7*$^{+/-}$ mice, which showed normal testis size and histology at 8 weeks (Supplemental Fig. 2E, F), were used as controls in subsequent analyses

To examine the temporal dynamics of Sertoli cell polarity establishment, we analyzed seminiferous tubule morphology across the first wave of spermatogenesis, from postnatal day (P)10 to P35. To specifically assess the role of MAP7 in Sertoli cells while minimizing contributions from germ cells, our analysis focused on stages up to P23, before MAP7 expression becomes detectable in step 9–11 spermatids (Fig. 1), to exclude potential secondary effects resulting from MAP7 loss in germ cells. In *Map7*$^{+/-}$ testes, seminiferous tubules were closed at P10, with early primary spermatocytes already evident (Fig. 2A, B). By P15, lumina were present in 13.2% of tubules, increasing to 81.2% by P17, coinciding with the appearance of pachytene spermatocytes. By P21, lumina were detected in 96.7% of tubules and became nearly ubiquitous thereafter (Fig. 2A, B). These findings are consistent with previous reports indicating that Sertoli cell polarization and BTB formation begin around P15–P17, concurrent with pachytene spermatocyte development (Russell et al. 1989; Willems et al. 2010), and suggest that Sertoli cells complete polarity establishment by P21. In contrast, *Map7*$^{-/-}$ tubules appeared morphologically normal at P10 but failed to form lumina between P15 and P28. By P35, multi-lumen structures or abnormally formed lumina were observed (Fig. 2A, B). These observations demonstrate that MAP7 is essential for seminiferous tubule remodeling and implicate it in apical domain formation during Sertoli cell polarization.

Directly assessing Sertoli cell adhesion and morphology is challenging due to the intimate association between Sertoli and germ cells within the seminiferous epithelium. To overcome this, we used serial sectioning and scanning electron microscopy (SEM). In P10 *Map7*$^{+/-}$ mice, 89.3% (25/28) of Sertoli cells adhered to the basement membrane, but only 60.7% (17/28) of Sertoli nuclei were positioned basally (Fig. 2C). By P21, all Sertoli cells adhered (12/12), and 91.7% (11/12) of their nuclei were basal (Fig. 2C). To quantify nuclear positioning in a larger cohort, we performed SOX9 immunostaining. The results showed a similar trend, with basal nuclei increasing to 80.5% from P10 to P17 (Fig. 2D, E; Supplemental Fig. 3A). These findings suggest that at P10, many Sertoli cells exhibit incomplete apical–basal compartmentalization, which progressively matures. Consistent with progressive polarization and lumen formation, Sertoli cells adhering to the basement membrane underwent distinct

morphological changes over time (Fig. 2C). In transverse views, Sertoli cells extended apically from P10 to P21 (Fig. 2C) and elongated along the longitudinal axis, suggesting that Sertoli cell polarity is established along both apical–basal and longitudinal axes during development. In *Map7*$^{-/-}$ mice, Sertoli cell adhesion and nuclear positioning were markedly impaired (Fig. 2C–E; Supplemental Fig. 3A). At P10, 59.5% (22/37) of Sertoli cells adhered to the basement membrane, and only 54.1% (20/37) of their nuclei were basal. By P21, adhesion further decreased, with only 31.6% (6/19) of Sertoli cells attached and 26.3% (5/19) of nuclei basally positioned (Fig. 2C). SOX9 immunostaining revealed a similar trend: the proportion of basal nuclei was 24.9% at P10 and declined to 18.2% at P17 (Fig. 2D, E; Supplemental Fig. 3A), indicating failed apical–basal compartmentalization in *Map7*$^{-/-}$ Sertoli cells. This defect persisted into adulthood (Supplemental Fig. 3B, C). Additionally, in P21 *Map7*$^{-/-}$ mice, Sertoli cells that adhered to the basement membrane failed to elongate in either axis, and apical extension was absent (Fig. 2C), reflecting severe loss of polarity and apical domain formation. In P10 *Map7*$^{+/-}$ mice, luminal F-actin signals were detected but disappeared by P17, coinciding with lumen formation (Fig. 2D; Supplemental Fig. 3A). In contrast, in *Map7*$^{-/-}$ mice, luminal F-actin signals persisted at P17, consistent with histological evidence of closed lumina (Fig. 2D; Supplemental Fig. 3A). These findings suggest that MAP7 is required for actin cytoskeletal remodeling during apical domain formation.

Sertoli cells and male germ cell lineages interact closely within the seminiferous tubules (Flanagan et al. 1991; Hiort et al. 2000; Ferlin et al. 2006; Naughton et al. 2006; Bashamboo et al. 2010). To determine whether MAP7 regulates Sertoli cell polarity in a male germ cell lineage-dependent or -independent manner, we examined Sertoli cell nuclear orientation after busulfan-induced depletion of spermatogonial stem cells (SSCs). Busulfan was administered at P28, and testes were analyzed 6 weeks later, after complete elimination of germ cell lineages. Following treatment, *Map7*$^{+/-}$ mice showed testis-to-body weight ratios comparable to untreated *Map7*$^{-/-}$ mice (Supplemental Fig. 3D), and hematoxylin-eosin (HE) staining confirmed germ cell depletion (Fig. 2F; Supplemental Fig. 3E). In *Map7*$^{+/-}$ testes, most Sertoli nuclei remained basally positioned, indicating that once apical–basal polarity is established, it is stably maintained even in the absence of germ cells. In contrast, *Map7*$^{-/-}$ Sertoli nuclei were frequently misoriented toward the lumen under the same conditions (Fig. 2F; Supplemental Fig. 3E), suggesting that polarity defects in *Map7*-deficient Sertoli cells occur independently of germ cell presence.

Collectively, these results demonstrate that MAP7 is indispensable for the establishment of Sertoli cell polarity and apical domain formation. Loss of MAP7 disrupts

cytoskeletal remodeling, nuclear positioning, and cell elongation, impairing lumen formation and seminiferous tubule architecture.

**MAP7 facilitates microtubule remodeling, but not microtubule stabilization, to establish Sertoli apical domain**

Our analysis showed that Sertoli cells attach to the basement membrane and establish polarity between P10 and P21, a process dependent on MAP7. To investigate cytoskeletal remodeling and MAP7 localization during polarization, we examined two major cytoskeletal components—microtubules and actin filaments at P10 (before polarization) and P17 (onset of polarization). At P10, microtubules, actin filaments, and MAP7-EGFP$^{KI}$ accumulated on the inner side of the seminiferous tubules and extended toward the basement membrane (Fig. 3A, top). By P17, these inner cytoskeletal components disappeared. Microtubules aligned along the luminal–basal axis, and actin filaments reorganized into the basal ES near the basement membrane (Fig. 3A, bottom). Consistent with observations in adult testes (Fig. 1A, C), MAP7 exhibited polarized distribution along microtubules, becoming enriched toward the luminal side (Fig. 3A, bottom). These results indicate that cytoskeletal remodeling, including luminal MAP7 accumulation, occurs after P10 as Sertoli cells establish polarity.

We next examined the impact of *Map7* deletion on cytoskeletal remodeling during Sertoli cell polarization. Previous studies reported reduced microtubule bundles in Sertoli cells of *Map7* gene-trap mice at P21 (Komada et al. 2000). As shown above, Sertoli microtubules undergo extensive reorganization between P10 and P17 (Fig. 3A). In *Map7*$^{+/-}$ mice, microtubules on the inner side of the tubules, which were prominent at P10, were lost by P17 (Fig. 3B). In contrast, in *Map7*$^{-/-}$ mice, inner microtubule signals persisted at P17, resembling the P10 pattern in wild-type and *Map7*$^{+/-}$ mice (Fig. 3A, top; Fig. 3B, bottom). Although actin filaments relocated to form the basal ES by P17 in control mice (Fig. 3A, bottom; Fig. 3B, top), they remained abnormally accumulated on the luminal side in *Map7*$^{-/-}$ mice (Fig. 3A, bottom). These findings suggest that Sertoli cells fail to transition beyond a P10-like cytoskeletal organization in the absence of MAP7, indicating the importance of MAP7 in cytoskeletal remodeling during polarization.

In *Map7*$^{+/-}$ mice, Sertoli microtubules extended along the luminal–basal axis (Supplemental Fig. 4A, top). In *Map7*$^{-/-}$ mice, although microtubule staining intensity was preserved, alignment was disrupted (Supplemental Fig. 4A, bottom). Similarly, actin filaments forming the apical ES were present in *Map7*$^{+/-}$ testes but replaced by ectopic actin structures in *Map7*$^{-/-}$ mice (Supplemental Fig. 4A, bottom). These results suggest that MAP7 promotes

microtubule alignment rather than stabilization, thereby organizing the cytoskeletal framework.

Since cytoskeletal organization is essential for apical domain formation, we examined whether MAP7 is required for the assembly of Sertoli cell junctional structures. In the testis, tight junctions reside at the basal side of Sertoli cells and contribute to BTB formation, partitioning the seminiferous epithelium into basal and luminal compartments. We then performed SEM to examine the effects of *Map7* KO. In P21 *Map7*$^{+/-}$ testes, electron-dense regions along the basal side of Sertoli–Sertoli junctions corresponded to tight junctions closely associated with the endoplasmic reticulum, consistent with previous reports (Luaces et al. 2023) (Fig. 3C; Supplemental Fig. 4B). The region immediately apical to the tight junctions likely represents adherens junctions, which were also associated with the endoplasmic reticulum. Unlike tight junctions, these regions displayed wider intercellular spaces, reflecting the looser membrane apposition typical of adherens junctions, though they could not be definitively distinguished from gap junctions or desmosomes based on morphology alone (Fig. 3C; Supplemental Fig. 4B). At P10, both *Map7*$^{+/-}$ and *Map7*$^{-/-}$ testes lacked clearly defined tight junctions and adherens junction–like structures (Fig. 3C; Supplemental Fig. 4B). In P21 *Map7*$^{-/-}$ mice, Sertoli cells formed expanded basal tight junctions but failed to establish adherens junction–like structures (Fig. 3C; Supplemental Fig. 4B). Consistent with these ultrastructural findings, ZO-1, a tight junction marker, localized specifically to the basal ES, marked by F-actin, in *Map7*$^{+/-}$ testes (Fig. 3D; Supplemental Fig. 4C). In *Map7*$^{-/-}$ testes, ZO-1 mislocalized to ectopic F-actin-rich regions (Fig. 3D; Supplemental Fig. 4C). β-catenin, a core adherens junction component, colocalized with F-actin at junctional regions near the basal ES in *Map7*$^{+/-}$ testes (Fig. 3B; Supplemental Fig. 4A). In *Map7*$^{-/-}$ testes, β-catenin accumulated on the luminal side, reflecting mislocalization of actin and microtubules (Fig. 3B; Supplemental Fig. 4A). Together, these results show that MAP7-dependent microtubule remodeling coordinates cytoskeletal architecture and junctional complex assembly, enabling apical domain formation during Sertoli cell polarization.

**MAP7 mediates cytoskeletal cross-talk by forming a complex with actomyosin components**

MAP7 promotes microtubule remodeling during Sertoli cell polarization, potentially by orchestrating broader cytoskeletal reorganization. To elucidate the molecular basis of this activity, we identified MAP7-interacting proteins using comparative immunoprecipitation-mass spectrometry (IP-MS). We analyzed two datasets: one from *MAP7-egfp*$^{KI}$ HeLa cells (Fig. 4A) and another from testes of P17–P20 *Map7-egfp*$^{KI}$ mice (Fig. 4B). *MAP7-egfp*$^{KI}$ HeLa cells were used as a complementary system, providing sufficient material and a controlled environment for

robust detection of MAP7-associated proteins. Comparison of IP-MS results between *MAP7-egfp*$^{KI}$ HeLa cells and P17–P20 *Map7-egfp*$^{KI}$ testes allows identification of MAP7-associated proteins that are specific to polarized Sertoli cells, whereas proteins detected in both systems likely represent general MAP7-associated proteins. The kinesin-1 heavy chain KIF5B, a known MAP7 interactor, was detected in both datasets, validating the robustness of our IP-MS approach. Comparative analysis identified 22 proteins that specifically co-immunoprecipitated with MAP7 in P17–P20 testes (Fig. 4C). Functional enrichment analysis via Metascape revealed significant overrepresentation of categories, such as motor proteins and Rho GTPase effectors (Fig. 4D). Based on these categories, we focused on cytoskeletal regulators among the 22 candidates (Fig. 4E), including TUBB3, NMII heavy chains MYH9 and MYH10, and vimentin (VIM), a key intermediate filament protein.

We prioritized MYH9 for further study due to its strong enrichment and established role in cytoskeletal remodeling. We examined MYH9 localization during Sertoli cell polarization and its dependence on MAP7. MYH9 was selectively enriched at luminal regions where microtubules and F-actin co-localized but was absent from areas lacking either component (Fig. 4F; Supplemental Fig. 5). In *Map7*$^{-/-}$ testes, microtubule and F-actin structures persisted in luminal regions where they are typically cleared during polarization; however, MYH9 failed to localize to these ectopic domains and instead remained diffusely distributed in the cytoplasm (Fig. 4F; Supplemental Fig. 5). These findings indicate that MYH9 localization at the luminal interface depends on MAP7, and suggest that MAP7 helps coordinate microtubules and F-actin, potentially via its association with NMII heavy chains.

**Functional differentiation of Sertoli cells is largely preserved in the absence of MAP7**

We showed that MAP7-mediated cytoskeletal remodeling establishes the Sertoli apical domain, which forms a structural scaffold for seminiferous epithelium organization. To determine whether loss of MAP7 affects functional differentiation of Sertoli cells, we performed scRNA-Seq at P19. GFP-positive Sertoli cells were isolated using a *Sox9-ires-gfp* allele combined with fluorescence-activated cell sorting (FACS) (Supplemental Fig. 6A). Germ cell contamination was detected despite efficient dissociation and library construction using the 10x Genomics platform. Hence, Sertoli cell-specific transcriptomes were extracted based on *Gata4*, *Sox9*, *Kitl*, and *Dhh* expression, yielding 311 control and 434 *Map7*$^{-/-}$ Sertoli cells (Supplemental Fig. 6B).

UMAP clustering identified six distinct clusters (C0–C5) (Fig. 5a). Gene enrichment analysis using Metascape revealed functional specialization among these clusters (Fig. 5B;

Supplemental Fig. 7). Cluster C0 was enriched for genes involved in responses to chemical stress, defining a subtype equipped for multifaceted protection against oxidative and metabolic stress through coordinated regulation of metabolic activity, mitochondrial function, proteostasis, cytoskeletal integrity, and gene regulation. C1 showed upregulation of fructose metabolism–related genes, suggesting a metabolically active population with enhanced mitochondrial and antioxidant capacity. C2 expressed genes associated with the establishment and maintenance of cell polarity, representing a dynamic population responsive to cues within the spermatogenic niche. C3 was enriched for genes involved in cytoskeletal dynamics and TGFβ signaling, implicating it in extracellular matrix (ECM) remodeling, growth factor signaling, and cell proliferation control. C4 expressed ECM-related genes, indicating a structurally specialized subtype engaged in ECM synthesis and blood–testis barrier (BTB) maintenance. C5 co-upregulated stress response and carbon metabolism genes, suggesting a high-energy, stress-adapted state that supports spermatogenesis via mitochondrial activity, antioxidant defense, and protein homeostasis mechanisms. To reconstruct differentiation trajectories among the six Sertoli cell clusters, we reanalyzed the datasets using Monocle3, which incorporates branch-aware pseudotime inference. Cluster C1 was selected as the root based on shared specificity and entropy scores, consistent with its metabolically active and transcriptionally diverse profile (Fig. 5B, C; Supplemental Fig. 7). While the overall trajectories appeared altered, the proportion of *Map7*$^{-/-}$ Sertoli cells with very low pseudotime values was only modestly increased (Fig. 5D). Comparison with controls showed that the average node degree was nearly identical (Fig. 5C), indicating that the local graph structure, reflecting connectivity among neighboring cells, remained largely intact. Minor differences in branch points and graph diameter likely reflect inherent variability in the data rather than major topological changes (Supplemental Fig. 6B). Consistent with this, the relative proportions of the six clusters showed only modest shifts, suggesting that the overall architecture of Sertoli cell differentiation is largely preserved in the absence of MAP7.

**Sertoli apical domain ensures orderly progression through the pachytene stage during meiosis**

Our analyses showed that MAP7 coordinates the remodeling of microtubule and actin networks and regulates the formation of junctional structures. While MAP7 is essential for apical domain formation and its disruption alters specific aspects of Sertoli cell function, the overall functional differentiation of Sertoli cells is largely preserved in its absence. Sertoli cell adhesion generates the stem cell niche for SSCs (Oatley et al. 2011; Hofmann and McBeath 2022). To assess this

further, we quantified SSCs in 8-week-old *Map7*$^{+/-}$ and *Map7*$^{-/-}$ mice. GFRα1$^{+}$ SSCs were not reduced in *Map7*$^{-/-}$ mice compared to those in *Map7*$^{+/-}$ controls (Fig. 6A, B), suggesting that Sertoli cells can still support the SSC niche despite the loss of adherens junctions, gap junctions, and apical domain, provided tight junctions are present. We next examined spermatogenic progression in 8-week-old *Map7*$^{+/-}$ and *Map7*$^{-/-}$ mice using ZFP541, a marker expressed from pachytene spermatocytes to round spermatids. Cell populations were quantified based on nuclear morphology and SYCP3 co-expression. In *Map7*$^{-/-}$ testes, both pachytene spermatocytes and round spermatids were reduced, with a more pronounced decrease in round spermatids (Fig. 6C, D; Supplemental Fig. 8A). To determine whether this reduction was due to increased cell death, we performed TUNEL staining. No apoptotic cells were observable in either genotype Supplemental Fig. 8B), indicating that round spermatid reduction cannot be attributable to cell death but instead suggests delayed differentiation into the round spermatid stage.

To assess the impact of apical domain disruption on germ cell development, we performed scRNA-Seq at P23, a stage preceding the appearance of step 9–11 spermatids (Supplemental Fig. 8C). This timing enabled focused analysis on earlier spermatogenic populations. At this stage, phenotypes observed in *Map7*$^{-/-}$ testes, including luminal closure, abnormal microtubule organization, and ectopic accumulation of F-actin and β-catenin, remained evident (Supplemental Fig. 8C, D). We dissociated whole testes from *Map7*$^{+/-}$ and *Map7*$^{-/-}$ mice and performed scRNA-Seq using the 10x Genomics platform. Germ cells were identified by *Ddx4* expression, yielding 1,914 *Map7*$^{+/-}$ and 4,745 *Map7*$^{-/-}$ germ cells (Supplemental Fig. 9). After dataset integration and unsupervised clustering, we identified 15 clusters (clusters 0–14; Supplemental Fig. 10A). To define germ cell differentiation stages, we used stage-specific marker analysis and RNA velocity profiling (Supplemental Fig. 10B, C). Metascape analysis revealed distinct biological processes enriched in each cluster, aligned with the expected progression of spermatogenesis (Supplemental Fig. 11). Based on inferred trajectory positions, clusters were renamed Ca–Co to reflect their differentiation order (Fig. 6E; Supplemental Fig. 10A). We then quantified the proportion of cells in each cluster to assess genotype-specific changes. To determine whether cluster expansion reflected aberrant meiotic entry, we examined expression of *Stra8* and *Meiosin*, key meiotic inducers (Ishiguro et al. 2020). Both genes were appropriately upregulated at meiotic entry and downregulated thereafter in *Map7*$^{-/-}$ germ cells, consistent with *Map7*$^{+/-}$ controls (Supplemental Fig. 12A). STRA8 protein levels were similarly unchanged between genotypes (Supplemental Fig. 12B), indicating that meiotic initiation and early transcriptional programs remained intact. Despite appropriate

meiotic entry, cytological assessment showed delayed progression in *Map7*$^{-/-}$ testes, with significantly fewer seminiferous tubules containing round spermatids compared to *Map7*$^{+/-}$ controls (Supplemental Fig. 12C, D). To clarify the identity of expanded clusters Cg and Ci in *Map7*$^{-/-}$ testes, we analyzed the expression of *Prelid1* and *Ccna1*, which mark early and late pachytene stages, respectively. *Prelid1* is expressed through early pachytene, and its downregulation marks the transition to mid-pachytene (Watanabe et al. 2015), whereas *Ccna1* expression increases during late pachytene and remains high into diplotene (Sweeney et al. 1996). *Prelid1* expression extended through Cg, indicating that Cg represents early pachytene cells expanded in *Map7*$^{-/-}$ testes (Fig. 6G). *Ccna1* was elevated in Ci of *Map7*$^{-/-}$ testes, whereas in *Map7*$^{+/-}$ testes, it was restricted to Cj, identifying Ci as a late pachytene population unique to *Map7*$^{-/-}$ mice. Notably, trajectory inference indicated that the Ci cluster in *Map7*$^{-/-}$ testes progresses to Ck (diplotene) through an alternative route that bypasses the Cj stage, as observed in *Map7*$^{+/-}$ mice (Fig. 6G). Together, these findings demonstrate that the Sertoli apical domain is essential for guiding orderly progression through the pachytene stage of meiosis.

## Discussion

We identified MAP7 as a key regulator of Sertoli cell polarity and apical domain formation, revealing a previously unrecognized molecular nexus that integrates microtubule dynamics with cytoskeletal cross-talk to support spermatogenesis. Although the importance of Sertoli cell polarization in testicular architecture and germ cell development is well established (O'Donnell et al. 2022), the molecular mechanisms underlying microtubule remodeling in this context have remained poorly defined. We showed that MAP7 is enriched at apical microtubules in Sertoli cells, where it orchestrates microtubule remodeling, a function distinct from stabilization, to support polarity. This remodeling is essential for the spatial coordination of F-actin, mediated in part through complexes involving NMII heavy chains (MYH9 and MYH10). Our biochemical analyses demonstrate that MAP7 forms complexes with MYH9/10, supporting a model in which MAP7 acts as a scaffold bridging microtubules and the actomyosin cytoskeleton. Disruption of this network in *Map7*$^{-/-}$ Sertoli cells leads to impaired cytoskeletal coordination, abnormal morphology, selective loss of junctional structures (excluding tight junctions), and failure of lumen formation.

We further showed that MYH9 is enriched at luminal regions where microtubules and F-actin co-localize—a pattern lost in *Map7*$^{-/-}$ Sertoli cells. Notably, MYH9 fails to accumulate even at ectopic sites where microtubules and F-actin are present, indicating that MAP7-mediated integration is required for NMII localization. This spatial regulation resembles NMII behavior in other epithelia. In the nephric duct and ureteric bud, NMII accumulates apically to support constriction and E-cadherin–mediated adhesion (Haque et al. 2017). Similarly, in dental epithelium, apical MYH9 facilitates convergent cell movement and stable adhesion for invagination (Du et al. 2024). Analogously, MAP7-dependent scaffolding in Sertoli cells recruits MYH9/10 to the apical domain, enabling F-actin remodeling and robust junction formation. The inability of *Map7*$^{-/-}$ Sertoli cells to recruit MYH9 despite intact microtubules and F-actin suggests that MAP7 not only scaffolds these elements but also creates a microenvironment encouraging NMII complex assembly and activity.

Our findings extend previous work implicating actin regulators, such as RAC1 and CDC42, in Sertoli cell polarity by highlighting microtubule remodeling as a complementary and indispensable mechanism (Heinrich et al. 2020; Heinrich et al. 2021). Unlike previous studies that focused on actin dynamics, our identification of MAP7-driven microtubule remodeling as a key driver of Sertoli apical domain formation reveals an essential aspect of cytoskeletal integration in epithelial organization. In *Map7*$^{-/-}$ Sertoli cells, adherens and gap junctions are disrupted, whereas tight junctions are abnormally expanded, indicating imbalanced junctional

composition and spatial organization. Although we did not directly assess BTB permeability, the loss of adhesion and communication junctions, both critical to BTB function, suggests that MAP7 deficiency may compromise its integrity. As BTB assembly depends on coordinated localization of multiple junction types, mislocalization of tight junctions alone is unlikely to preserve barrier function. Thus, MAP7 appears essential for establishing the structural foundation of a functional BTB, though further studies are needed to define the extent of impairment.

Sertoli cells form the SSC niche through BTB construction and secretion of trophic factors that support SSC maintenance and differentiation (Oatley et al. 2011; Hofmann and McBeath 2022). Sertoli cell polarity determines the spatial organization of junctions and shapes the microenvironment required for germ cell development. Although polarity loss has been linked to impaired niche function, our data showed that in *Map7*$^{-/-}$ Sertoli cells, tight junctions are retained but ectopically formed, whereas adherens junctions fail to assemble. Despite these abnormalities, SSC numbers remain unchanged throughout the eight weeks, and the first wave of spermatogenesis proceeds without overt defects in spermatogonial differentiation. These findings suggest that tight junctions (even when mislocalized) may be sufficient to support early spermatogenesis, and that canonical apical domain architecture is not essential for SSC maintenance during the postnatal period. In addition, even after germ cell depletion by busulfan treatment, *Map7*-deficient Sertoli cells failed to reestablish basal nuclear positioning, indicating that loss of MAP7 causes an intrinsic polarity defect. These findings suggest that MAP7 acts as a cell-autonomous regulator of Sertoli cell polarity, rather than mediating effects indirectly through germ cell–Sertoli cell interactions.

Our scRNA-Seq analyses showed that despite severe defects in polarity and apical domain formation, the intrinsic transcriptional differentiation programs of Sertoli cells are largely maintained in *Map7*$^{-/-}$ mice. This suggests that MAP7 primarily influences spatial and structural organization rather than core cellular identity. Thus, Sertoli apical domain architecture may govern the germ cell niche through spatial rather than transcriptional regulation, explaining the delayed meiotic progression observed in *Map7*-deficient testes. This delay occurs in the absence of increased apoptosis or defects in meiotic initiation, implicating the apical domain as a critical structural niche component that ensures timely progression through meiosis. Given the reliance of germ cells on Sertoli-derived structural and trophic support, our data suggest that microtubule-driven apical remodeling orchestrates key intercellular interactions required for germ cell differentiation.

In summary, MAP7 is a master regulator of Sertoli cell polarity that promotes

seminiferous tubule morphogenesis and spermatogenic progression through microtubule remodeling and cytoskeletal coordination. By forming complexes with MYH9/10, MAP7 facilitates cytoskeletal cross-talk essential for epithelial polarization. Although this mechanism may reflect a broader principle of epithelial organization, Sertoli cells possess distinctive polarity features and junctional architectures not found in typical columnar epithelia. Consistent with this, loss of the MAP7 homolog Ensconsin in *Drosophila* disrupts planar cell polarity without affecting apico-basal polarity (Kikuchi et al. 2018), suggesting that MAP7-dependent scaffolding functions are highly context-dependent and may govern different aspects of epithelial organization depending on cell type. Despite these insights, our study has several limitations. First, although we demonstrated the role of MAP7 in Sertoli cell polarity and junctional organization using mouse models, it remains unclear whether this mechanism is conserved across other mammalian epithelia. Given the specialized architecture of Sertoli cells and prior evidence of context-dependent MAP7 function in invertebrate systems, further studies are required to assess the generality of these findings. Second, although we characterized Sertoli cell polarization in fixed tissues, real-time analysis at ultrastructural resolution remains highly challenging due to the dense packing and complex morphology of Sertoli cells. To overcome these difficulties, we employed SEM-based array tomography to reconstruct individual cell architecture (Fig. 2C). However, achieving comparable resolution in live imaging—particularly without mosaic labeling to clearly delineate single cells within this crowded environment—remains a formidable technical barrier. Overcoming this limitation is essential to fully elucidate MAP7's dynamic role in polarity establishment. Finally, while we evaluated the impact of MAP7 loss on Sertoli cell architecture and early germ cell development, the long-term consequences for fertility, BTB integrity, and testicular homeostasis remain unknown. Future studies incorporating live imaging, temporally controlled gene perturbation, and cross-epithelial comparisons will be critical to fully define the roles of MAP7 in epithelial polarity and its relevance to reproductive and barrier-related disorders.

## Materials and Methods

### Animals

C57BL/6NJcl mice were purchased from CLEA Japan (Tokyo, Japan). We used *Map7*$^{+/-}$, *Sox9-ires-gfp;Map7*$^{+/-}$, and *Map7-egfp*$^{KI}$ mice, all maintained on a C57BL/6 background, for this study. The *Sox9-ires-gfp* mouse line was originally generated by Nel-Themaat *et al*. (Nel-Themaat et al. 2009). For scRNA-Seq of total testis cells, *Map7*$^{+/-}$ or *Map7*$^{-/-}$ male mice at P23 were used. For scRNA-Seq targeting Sertoli cells, *Sox9-ires-gfp* or *Sox9-ires-gfp; Map7*$^{-/-}$ male mice at P19 were used. Testes collected from mice at P10–P35 and at 8 weeks of age were used for histological and immunostaining analyses. Whenever possible, KO animals were compared with littermates or age-matched non-littermate controls from the same colony, unless otherwise specified. Mice were housed under standard conditions in a temperature- and light-controlled facility (12-hour light/dark cycle; 22□±□1□°C). All animal procedures were approved by the Institutional Animal Care and Use Committee (approval numbers: A2019-127, A2021-018, A2023-036, and A2025-018) and conducted in accordance with institutional guidelines.

### Cell culture

Wild-type and *MAP7-EGFP*$^{KI}$ HeLa cells were cultured in Dulbecco's Modified Eagle Medium (DMEM, 043-30085; Fujifilm Wako Pure Chemical, Osaka, Japan) supplemented with 10% fetal bovine serum (FBS, 35-015-CV; Corning, Corning, NY, USA) and penicillin–streptomycin (26253-84; Nacalai, Kyoto, Japan) at 37 °C in a humidified atmosphere containing 5% CO□ (Kikuchi et al. 2018).

### crRNAs and genotyping primers

The sequences of crRNAs and genotyping primers used in this study are provided in Supplemental Tables 1 and 2, respectively.

### Generation of *Map7*$^{+/-}$ mice and genotyping

*Map7*$^{+/-}$ mice were generated by introducing Cas9 protein (317-08441; NIPPON GENE, Toyama, Japan), tracrRNA (GE-002; FASMAC, Kanagawa, Japan), and synthetic crRNA (FASMAC) into C57BL/6N fertilized eggs via electroporation. To generate the *Map7* exon2–8 deletion (Ex2-8Δ) allele, synthetic crRNAs were designed to target the sequences

GGACAAACTAGCAACCACTC(AGG) in exon 2 and CGCCTGAGGGCTCTGCACGA(AGG) in exon 8 of the *Map7* gene.

The electroporation mixture consisted of tracrRNA (10 μM), synthetic crRNA (10 μM), and Cas9 protein (0.1 μg/μL) in Opti-MEM I Reduced Serum Medium (31985062; Thermo Fisher Scientific, Waltham, MA, USA). Electroporation was performed using the Super Electroporator NEPA 21 (NEPA GENE, Chiba, Japan) on glass microslides with round wire electrodes (1.0 mm gap, 45-0104; BTX, Holliston, MA, USA). The procedure included four steps of square-wave pulses: (1) three poring pulses of 3 ms each at 30 V with 97 ms intervals; (2) three polarity-reversed poring pulses of 3 ms each at 30 V with 97 ms intervals; (3) five transfer pulses of 50 ms each at 4 V with 50 ms intervals and 40% decay in voltage per pulse; and (4) five polarity-reversed transfer pulses of 50 ms each at 4 V with 50 ms intervals and 40% decay in voltage per pulse.

The targeted *Map7* Ex2-8Δ allele in F0 mice was identified via PCR using the following primers: *Map7*_C1F (5′-TAATGCAGGACCAGTCACTCTGCTGAACAG-3′) and *Map7*_C2R (5′-CTGTCACCTGATCTTGTACCCA-3′) for the KO allele (366 bp); *Map7*_C1F and *Map7*_C1R (5′-TAAGAACAGTAACTGCCCTTGCAGAGGACC-3′) for the exon 2 of the wild-type allele (597 bp); or Map7_C2F (5′-ACCTGCACTCTAGTTATCCCCA-3′) and *Map7*_C2R for the exon 8 of the wild-type allele (228 bp). PCR amplicons were confirmed using Sanger sequencing. Genotyping PCR was routinely performed as follows. Genomic DNA was prepared by incubating a small piece of the cut toe in 180 μL of 50 mM NaOH at 95 °C for 15 min, followed by neutralization with 20 μL of 1 M Tris-HCl (pH 8.0). After centrifugation for 20 min, 1 μL of the resulting DNA solution was used as the PCR template. Each reaction (8 μL total volume) contained 4 μL of Quick Taq HS DyeMix (DTM-101; Toyobo, Osaka, Japan) and a primer mix. PCR cycling conditions were as follows: 94 °C for 2 min; 35 cycles of 94 °C for 30 s, 65 °C for 30 s, and 72 °C for 1 min; followed by a final extension at 72 °C for 2 min and a hold at 4 °C. PCR products were analyzed using agarose gel electrophoresis. This protocol was also applied to other mouse lines and alleles generated in this study.

**Generation of *Map7-egfp* knock-in mice and genotyping**

*Map7-egfp*$^{KI}$ mice were generated using the PITCh system, as previously described (Sakuma et al. 2016). Cas9 protein, tracrRNA, synthetic crRNA, and the PITCh vector were introduced into C57BL/6N fertilized eggs via electroporation. The synthetic crRNA was designed to target the sequence ACTCATATAACTTCTACATG(AGG) within the Map7 gene and GTGCTTCGATATCGATCGTT(TGG) within the PITCh vector.

The targeted *Map7-egfp*$^{KI}$ allele in F0 mice was identified by PCR using the following primers: *Map7-egfp*_C1F (5′-CTGACCTGTTCTTCCTACAGCA-3′) and *Map7-egfp*_C1R (5′-AGCCTGAAGTTCCATTCATTGT-3′) to amplify both the *Map7-egfp*$^{KI}$ allele (996 bp) and the wild-type allele (228 bp). To confirm 5′ integration of the *Map7-egfp*$^{KI}$ allele, primers *Map7-egfp*_C1F and *Map7-egfp*_E1R (5′-TTGTACAGCTCGTCCATGCCGAG-3′) were used to amplify a 935 bp fragment; for 3′ integration, *Map7-egfp*_E1F (5′-ACCACATGAAGCAGCACGACTTC-3′) and *Map7-egfp*_C1R were used to amplify a 548 bp fragment. All PCR amplicons were confirmed by sequencing.

**Immunoblotting**

For immunoblotting, testes were lysed in Laemmli sample buffer prepared in-house. After boiling, the lysates were separated by SDS–PAGE, transferred to polyvinylidene difluoride (PVDF) membranes (MilliporeSigma, Burlington, MA, USA), and immunoblotted with antibodies. Detection was performed using Amersham ECL Prime (RPN2236; Cytiva, Tokyo, Japan), and signals were visualized using the FUSION Solo imaging system (Vilber Lourmat, Marine, France). The following primary antibodies were used: mouse anti-Actin (C4, 0869100-CF; MP Biomedicals, Irvine, CA, USA), mouse anti-Clathrin heavy chain (610500; BD Biosciences, Franklin Lakes, NJ, USA), rat anti-GFP (GF090R; Nacalai, 04404-84), rabbit anti-MAP7 (SAB1408648; Sigma-Aldrich, St. Louis, MO, USA), rabbit anti-MAP7 (C2C3, GTX120907; GeneTex, Irvine, CA, USA), and mouse anti-α-tubulin (DM1A, T6199; Sigma-Aldrich). Corresponding HRP-conjugated secondary antibodies were used for detection: goat anti-mouse IgG (12-349; Sigma-Aldrich), goat anti-rabbit IgG (12-348; Sigma-Aldrich), and goat anti-rat IgG (AP136P; Sigma-Aldrich). Detailed information for all primary and secondary antibodies is provided in Supplemental Table 3.

**Histological analysis**

For HE staining, testes and epididymides were fixed in 10% neutral buffered formalin or in-house–prepared Bouin's solution, followed by paraffin embedding. Sections were cut at a thickness of 6 μm and mounted on CREST-coated glass slides (SCRE-01; Matsunami Glass, Osaka, Japan). After dehydration, sections were stained with HE using standard protocols.

For immunofluorescence, testes were fixed overnight at 4 °C in 4% paraformaldehyde in PBS, then cryoprotected by immersion in 10%, 20%, and 30% sucrose solutions at 4 °C. Tissues were briefly incubated in OCT compound (4583; Sakura Finetechnical, Tokyo, Japan) at room temperature, embedded in OCT, and snap-frozen in liquid nitrogen. Cryosections (10 μm

thick) were stored at −80 °C until use. Prior to staining, sections were washed once in PBS for 10 min and twice in 0.1% Triton X-100/PBS for 10 min each. Blocking was performed using 2.5% normal donkey serum (017-000-121; Jackson ImmunoResearch Laboratories, PA, USA) and 2.5% normal goat serum (005-000-121; Jackson ImmunoResearch Laboratories) in 0.1% Triton X-100/PBS for 1 h at room temperature. Sections were incubated with primary antibodies overnight at 4 °C and subsequently with Alexa Fluor-conjugated secondary antibodies (Thermo Fisher Scientific) for 1 h at room temperature. Detailed information on all primary and secondary antibodies is provided in Supplemental Table 3. For PNA lectin and phalloidin staining, FITC-conjugated *Arachis hypogaea* lectin (1:1000, L7381; Sigma-Aldrich) and Alexa Fluor 647-conjugated phalloidin (1:1000, A2287; Thermo Fisher Scientific) were used, respectively. TUNEL staining was performed using the MEBSTAIN Apoptosis TUNEL Kit Direct (8445; MBL, Tokyo, Japan) to detect apoptotic cells. Nuclei were counterstained with DAPI (D9542; Sigma-Aldrich) for 30 min at room temperature. Imaging was performed using a Leica TCS SP8 confocal microscope, and images were processed using LAS X software (version 2, Leica Microsystems, Vienna, Austria). Objectives used were HC PL APO 40×/1.30 OIL CS2 (11506428; Leica) and HC PL APO 63×/1.40 OIL CS2 (11506350; Leica), with digital zoom applied as needed for high-magnification imaging. DAPI was detected using PMT detectors, while Alexa Fluor 488, 594, and 647 signals were captured using HyD detectors. Images were acquired in sequential mode with detector settings adjusted to prevent signal bleed-through. Laser power and exposure settings were optimized for each experiment but kept constant during acquisition to ensure comparability across samples. Image brightness was adjusted linearly within a consistent dynamic range using Fiji software (v.2.16/1.54p; NIH) (Schindelin et al. 2012). For Fig. 6D, cell quantification was performed using Aivia software (version 14.1; Leica). Statistical analyses and graph generation were performed using Microsoft Excel (Microsoft Office LTSC Professional Plus 2021), except for ANOVA, which was conducted in R (version 4.4.0) (Team 2021). For ANOVA, linear models were fitted using the base **stats** package (lm function), and analysis of variance was performed with the **anova** function.

**Volume electron microscopy (array tomography)**

Immediately following euthanasia, testes were dissected from animals, immersed in half-strength Karnovsky fixative (2% paraformaldehyde, 2.5% glutaraldehyde in 0.1 M phosphate buffer, pH 7.3), bisected in fixative, and fixed for 48 h. The tissue was post-fixed with 1% osmium tetroxide in buffer, dehydrated in a graded ethanol series, and embedded in

EPON 812 resin using TAAB Embedding Resin Kit with DMP-30 (T004; TAAB Laboratory and microscopy, Berks, UK). After trimming to a 0.5 mm square, approximately 600 serial 50 nm ultrathin sections were collected on silicon wafers. Sections were stained with uranyl acetate and modified Sato's lead solution (Takagi et al. 1990) for 5 min each and subjected to SEM (JSM-IT800SHL; JEOL, Tokyo, Japan) to generate a stack of serial section images. Imaging was conducted at a pixel resolution of 5 nm × 5 nm, with two montaged images per section, each at 7680 × 5760 pixels. After alignment using Stacker Neo (version 3.5.3.0; JEOL), 1/2 or 1/4 binning was applied. Three-dimensional ultrastructural visualization and analysis were performed using Amira 2022 (version 2022.1; Thermo Fisher Scientific) and Microscopy Image Browser (version 2.91) (Belevich et al. 2016). For Fig.3C, regions of interest within the image stack were subsequently re-examined at a higher pixel resolution of 1.25 nm × 1.25 nm.

**Immunoprecipitation**

Wild-type and *MAP7-egfp*$^{KI}$ HeLa cells were lysed in a buffer containing 10 mM Tris-HCl (pH 7.5), 150 mM NaCl, 0.5 mM EDTA, and 0.5% NP-40, supplemented with complete protease inhibitor (4693116001; Roche Diagnostics, Mannheim, Germany). Testes were harvested from male C57BL/6 wild-type or *Map7-egfp*$^{KI}$ mice at P17–P20, detunicated, and homogenized in the same lysis buffer with protease inhibitors. Lysates were cleared by centrifugation at 100,000 × *g* for 10 min at 4 °C. To reduce nonspecific interactions, supernatants were precleared through incubation with 50 µL of ChromoTek control magnetic agarose beads (bmab; Proteintech, Rosemont, IL, USA) for 1 h at 4 °C with gentle rotation. The resulting supernatants were used as input material for immunoprecipitation. To isolate Map7/MAP7-EGFP$^{KI}$ complexes, 50 µL of ChromoTek GFP-Trap magnetic agarose beads (gtma; Proteintech) were added to the lysates. After incubation, the beads were washed thoroughly with lysis buffer, and bound proteins were eluted with 40 µL of elution buffer (100 mM Glycine-HCl, pH 2.5, 150 mM NaCl) and neutralized with 4 µL of 1 M Tris-HCl (pH 8.0).

**Mass spectrometry**

Immunoprecipitated proteins were separated on 4–12% NuPAGE gels (NP0321PK2; Thermo Fisher Scientific) and electrophoresed until they migrated approximately 1 cm from the loading wells. Gels were stained with SimplyBlue SafeStain (LC6060; Thermo Fisher Scientific), and protein-containing bands were excised and diced into approximately 1 mm pieces. Gel fragments were subjected to in-gel digestion: proteins were reduced with dithiothreitol (DTT; Thermo Fisher Scientific), alkylated with iodoacetamide (Thermo Fisher

Scientific), and digested overnight at 37 °C using trypsin and Lysyl endopeptidase (Promega, Madison, WI, USA) in 40 mM ammonium bicarbonate buffer (pH 8.0).

The generated peptides were analyzed using an Advanced UHPLC system (ABRME1ichrom Bioscience) coupled to a Q Exactive mass spectrometer (Thermo Fisher Scientific). Raw data were acquired using Xcalibur software (version 4.0.27.19; Thermo Fisher Scientific) and processed using Proteome Discoverer version 1.4 (Thermo Fisher Scientific) in combination with Mascot version 2.5 (Matrix Science, Boston, MA, USA). Searches were conducted against the SwissProt database (Bairoch and Apweiler 1999), restricted to entries for *Homo sapiens* or *Mus musculus*. A decoy database comprising randomized or reversed sequences was used to estimate the false discovery rate (FDR), and peptide identification confidence was evaluated using the Percolator algorithm. Peptide-spectrum matches were filtered to maintain a global FDR below 1%, ensuring high-confidence identifications. The complete LC-MS/MS dataset has been deposited in jPOST (Okuda et al. 2024) under the accession numbers PXD066392 (ProteomeXchange) and JPST003958 (jPOST).

**scRNA-Seq**

Testes were isolated from *Sox9-ires-gfp* and *Sox9-ires-gfp;Map7*$^{-/-}$ mice at P19, or from *Map7*$^{+/-}$ and *Map7*$^{-/-}$ mice at P23. The tissue was finely minced and digested with 1.2 mg/mL type I collagenase (Fujifilm Wako Pure Chemical) at 37 °C for 10 min, followed by centrifugation to collect tissue pellets. Pellets were incubated with Accutase (Innovative Cell Technologies, San Diego, CA, USA) for 5 min at 37 °C. The digestion was terminated by adding DMEM supplemented with 10% FBS, and the resulting cell aggregates were gently dissociated by pipetting. Cell suspensions were sequentially passed through 95 µm and 35 µm strainers (BD Biosciences, Milpitas, CA, USA) to remove debris and large clumps. Cells were pelleted by centrifugation, resuspended in PBS containing 0.1% bovine serum albumin, and sorted using a SH800 cell sorter (SONY, Tokyo, Japan) to exclude dead cells. GFP-positive cells were isolated for Sertoli cell-specific scRNA-Seq. Viable cells were resuspended in DMEM with 10% FBS. Approximately 7,000 single cells were loaded onto a Chromium controller (10x Genomics, Pleasanton, CA, USA) for droplet-based single-cell capture. Libraries were prepared using the Chromium Single Cell 3 Reagent Kits v3 (PN-1000075; 10x Genomics), following the manufacturer's protocol, and sequenced on an Illumina HiSeq X platform to generate 150 bp paired-end reads. Details on the number of mice used, total cells captured, mean reads per cell, sequencing saturation, number of genes detected per cell, median UMI counts per cell, and total cell numbers before and after quality control are provided in Supplemental Fig. 6B and

Supplemental Fig. 9A. Sequencing data have been deposited in the DDBJ Sequence Read Archive under accession number DRR709131, DRR709132, DRR709133, and DRR709134.

**Statistical analysis of scRNA-Seq**

Raw FASTQ files were processed and mapped to the mouse reference genome (mm10, GENCODE vM23/Ensembl 98) using the Cell Ranger pipeline (version 4.0, 10x Genomics). Subsequent analyses were performed using R (version 3.6.2) within the RStudio (team 2025) environment (version 1.2.1335). Quality control and primary data processing were conducted using the 'Seurat' package (version 3.2.2) in R (Butler et al. 2018) (Stuart et al. 2019). Cells expressing fewer than 200 genes were excluded to eliminate low-quality cells. Datasets were merged and normalized using Seurat's SCTransform function. Dimensionality reduction and clustering were performed using RunUMAP, with clustering based on FindNeighbors and FindClusters functions (default parameters). Differentially expressed genes were identified using FindAllMarkers (only.pos = TRUE, min.pct = 0.25, logfc.threshold = 0.25). FindMarkers was used with default parameters for specific pairwise comparisons.

Sertoli cell populations were isolated based on expression of gonadal supporting cell markers (*Gata4*, *Sox9*, *Kitl*, and *Dhh*). Selected cells were visualized using UMAP plots, and clusters expressing markers of other gonadal lineages or high mitochondrial gene content were excluded. Remaining cells were retained for downstream analysis as Sertoli cells.

Germ cells were selected based on *Ddx4* expression and re-visualized on UMAP plots. Clusters expressing somatic markers or showing high mitochondrial gene content were excluded. The remaining cells were analyzed as germ cells. RNA velocity analysis was performed using the Velocyto package (Python 3.7.3) following default settings (La Manno et al. 2018) and visualized using UMAP embeddings generated by Seurat.

**Gene enrichment analysis**

Gene enrichment analyses were performed using Metascape (Zhou et al. 2019) (v3.5.20250701) with default settings, and results were visualized in Microsoft Excel. To characterize each cluster, we used the top 100 representative genes per cluster.

**Statistics**

All experiments were repeated at least three times using biological replicates. Data are presented as mean ± standard deviation (S.D.) or, for box-and-whisker plots, as median, first and third quartiles, and 5th–95th percentiles. Statistical comparisons between groups were primarily

performed using the Student's *t*-test. A *P* value <0.05 was considered statistically significant. *Z*-scores for IP-MS analyses were calculated from Mascot scores. Spearman's correlation coefficients were computed to estimate transcriptional similarity between clusters. *P* values and adjusted *P* values (*padj*) during the estimation of Sertoli cell proportions per cluster were calculated using Fisher's exact test. One-way ANOVA was performed to assess statistical significance during the quantification of round spermatids and pachytene spermatocytes.

## Data Availability

The LC-MS/MS and scRNA-Seq datasets generated in this study have been deposited in public repositories. Accession numbers are listed in the Materials and Methods section of the main text.


## Acknowledgements

We thank Dr. Nishinakamura for generously providing the MYH9 antibody. We are also grateful to members of our laboratory for their insightful discussions and technical support. This work was partially conducted at the Center for Animal Resources and Development and the Research Facilities of the School of Medicine, Kumamoto University.


## Author contributions

K.K. designed the study, performed the majority of the experiments, interpreted the data, and wrote the manuscript. T.F. and N.M. contributed to the initial analysis of *Map7* KO mice. K.O. assisted with array tomography analysis. R.S. contributed to scRNA-Seq analysis. S.F. supported histological analysis. K.Y. and S.U. assisted with scRNA-Seq analyses. N.T. conducted the mass spectrometry analysis. A.N. provided advice on IP-MS analysis. K.A. generated the knock-in mice. K.I. provided technical assistance for mouse testis analyses. All authors discussed the results and reviewed the manuscript.


## Funding

This study was supported by the Research Program for the Inter-University Research Network for High Depth Omics and the Joint Usage/Research Program for Developmental Medicine, IMEG, Kumamoto University. Additional support was provided by JSPS KAKENHI (Grant Numbers 19K06664, 22K06226, 25K09632, JP16H06280 [ABiS], JP22H04922 [ABiS], and JP16H06276 [AdAMS]); the MEXT Promotion of Development of a Joint Usage/Research System Project: Coalition of Universities for Research Excellence (CURE) Program (Grant Number JPMXP1323015486); and grants from the Narishige Zoological Science Award, the Novartis Foundation for the Promotion of Science, the Mochida Memorial Foundation, the Takeda Science Foundation, and the Uehara Memorial Foundation (to K.K.). Further support was provided by MEXT KAKENHI (JP23H00379, 25H01304), AMED PRIME (21gm6310021h0003), and grants from the Naito Foundation, the Astellas Foundation, and the Takeda Science Foundation (to K.I.).

**Conflict of Interest**

The authors declare that the research was conducted in the absence of any commercial or financial relationships that could be construed as a potential conflict of interest.

## Figure legends

**Figure 1. MAP7 exhibits polarized localization to the apical side of microtubule bundles along the apical-basal axis in Sertoli cells.**

(**A**) Sections of seminiferous tubules from 8-week-old *Map7-egfp*$^{KI}$ mice were stained for GFP, β-III-tubulin (TUBB3), and DAPI. TUBB3 was used as a Sertoli cell-specific marker. The lower panel shows seminiferous tubules containing step 9–11 spermatids. Scale bar: 50 or 25 μm. (**B**) Sections of seminiferous tubules from 8-week-old *Map7-egfp*$^{KI}$ mice were stained for GFP, acetylated tubulin, and DAPI. The lower panel shows a magnified view of step 9 spermatids. Scale bar: 50, 25, or 10 μm. (**C**) Sections of seminiferous tubules from 8-week-old wild-type mice were stained for MAP7, TUBB3, and DAPI. The lower panel shows seminiferous tubules containing step 9–11 spermatids. Scale bar: 50 or 25 μm.

**Figure 2. MAP7 regulates the orientation and morphology of Sertoli cells along the apical-basal axis.**

(**A**) Hematoxylin and eosin staining of the sections from testes of the indicated mice (10-, 17-, 21-, 28-, or 35-days old). Biologically independent mice (N = 3) for the indicated genotype were examined. Scale bar: 100 μm. (**B**) The percentage of seminiferous tubules with lumens at the indicated time points was calculated. Data from more than 140 seminiferous tubules from mice (three independent experiments) are indicated and represent the average ± standard deviation (S.D.) (**C**). Array tomography images of seminiferous tubules in mice (10- or 21-day-old). Using a serial-section scanning electron microscope (SEM), 503, 588, 398, or 498 images were obtained at P10 or P21 from *Map7*$^{+/-}$ and *Map7*$^{-/-}$ mice, respectively. Sertoli cells (green), spermatogonia (orange), and spermatocytes (red) were identified based on their nuclear and cellular morphology and adhesion to the basement membrane during the examination of serial-section images. The number represents the ratio of Sertoli cells attached to the basement membrane (upper left, adherent) or Sertoli cell nuclei positioned in the basal layer (lower left, basal nuclei) to the total number of Sertoli cells observed in the stack file (right), providing a visual summary of the quantitative analysis described in the text. The three-dimensional images of Sertoli cells were constructed by manually segmenting serial-section images. Blue or yellow indicates Sertoli cells or basement membrane, respectively. T and L represent views from the transverse and longitudinal axes of the seminiferous tubules, respectively. Scale bar: 10 μm. (**D**) The orientation of Sertoli cell nuclei along the apical–basal axis and actin remodeling on the apical side were analyzed in mice (10- or 17-day-old). To view the orientation of Sertoli cell

nuclei along the apical–basal axis, seminiferous tubules were stained for DAPI and SOX9, allowing detection of Sertoli cell nuclei. Seminiferous tubule morphology was visualized with phalloidin (F-actin) staining. Scale bar: 25 μm. (**E**) The percentage of $SOX9^{+}$ Sertoli cells per cell layer at P10 and P17 was calculated. Data were obtained from more than 145 $SOX9^{+}$ Sertoli cells per mouse (from over ten images collected across three independent experiments) and are presented as mean□±□S.D. Statistical comparisons between *Map7*$^{+/-}$ and *Map7*$^{-/-}$ mice were performed for each corresponding layer at P17 using Student's t-test. All three layers showed significant differences between *Map7*$^{+/-}$ and *Map7*$^{-/-}$ mice (*, $P<2.20 \times 10^{\square\square}$). (**F**) The germ-independent polarity formation of Sertoli cells was analyzed by eliminating the male germ cell lineage with busulfan treatment. At 28 days old, mice were intraperitoneally injected with busulfan (45 μg/g) and dissected six weeks later for observation using hematoxylin and eosin staining. Biologically independent mice (N□=□4) of the specified genotype were examined. Scale bar: 50 μm.

**Figure 3. MAP7 facilitates microtubule remodeling, but not microtubule stabilization, to establish Sertoli cell polarity.**

(**A**) Seminiferous tubule sections derived from *Map7-egfp*$^{KI}$ mice (10- or 17-day-old) were stained for GFP, TUBB3, phalloidin (F-actin), and DAPI. Scale bar: 50 μm. (**B**) The direction and stabilization of microtubule bundles in Sertoli cells were analyzed using three-dimensional projection images from mice (17-day-old). Seminiferous tubule sections were stained with TUBB3 (β-III-tubulin), phalloidin (F-actin), β-catenin, and DAPI. Notably, the proportion of seminiferous tubules in *Map7*$^{-/-}$ mice where TUBB3, F-actin, and β-catenin were abnormally accumulated on the inner side of the tubules was consistent with the proportion of tubules lacking lumen formation, as shown in Fig. 2A, B. Scale bar: 50 or 25 μm. (**C**) High-resolution SEM images were acquired to analyze tight junction formation between Sertoli cells attached to the basement membrane in testes from 10- and 21-day-old mice. The black arrow indicates the Sertoli–Sertoli cell boundary at P10, while the magenta and blue arrows indicate tight junctions and adherens junction–like structures at P21, respectively. The asterisk marks the endoplasmic reticulum. Scale bar: 0.1 μm. (**D**) Tight junction formation of Sertoli cells was analyzed using three-dimensional projection images in mice (17-day-old). The percentage of seminiferous tubules with ectopic ZO-1 was calculated. Data are from more than 45 seminiferous tubules in mice (three independent experiments), and represent the average□±□S.D. Statistical significance is indicated by $P<0.002$ (Student's *t*-test). Scale bar: 25 μm.

**Figure 4. MAP7 mediates cytoskeletal cross-talk by forming a complex with actomyosin components.**

(**A**) Immunoprecipitation-mass spectrometry (IP-MS) analysis using *MAP7-egfp*$^{KI}$ HeLa cells. Lysates from wild-type HeLa cells were used as a negative control for immunoprecipitation (IP). Volcano plot of proteins identified in both control and Map7-EGFP$^{KI}$ IP samples, excluding keratin and immunoglobulin-derived proteins. Protein quantification was performed based on Mascot scores. Proteins with a log□ fold change (Map7-EGFP$^{KI}$ IP / Control IP) > 1 and a z-score > 2 are highlighted in red. Proteins, such as MVP, MAP7, and KIF5B, which had high scores on both metrics, are labeled. (**B**) IP-MS analysis using testes from P17–20 *Map7-egfp*$^{KI}$ mice. Lysates from age-matched wild-type testes were used as the negative control. Volcano plot of proteins identified in both control and MAP7-EGFP$^{KI}$ IP samples, with keratin and immunoglobulin-derived proteins excluded. Proteins with a log□ fold change > 1 and z-score > 2 are marked in red. Proteins, such as MAP7, MYH9, MYH10, and KIF5B, which had high scores on both metrics, are labeled. (**C**) A Venn diagram comparing interacting proteins identified in *MAP7-egfp*$^{KI}$ HeLa cells and P17–20 *Map7-egfp*$^{KI}$ testes. Ten common interactors were identified, including known MAP7-binding partners, such as KIF5B and its light chain KLC2, as well as TUBB4B, a beta-tubulin isoform. (**D**) Enrichment analysis using Metascape was performed on 22 Sertoli-specific MAP7-interacting proteins identified exclusively in P17–20 *Map7-egfp*$^{KI}$ testes. (**E**) Cytoskeleton-associated proteins that were below the detection limit in the Control-IP are highlighted. Sertoli cell-specific proteins are indicated in red. Proteins are classified based on their association with microtubules (MT), actin filaments (AF), or intermediate filaments (IF). The Mascot score represents a confidence metric generated by the Mascot search engine, indicating the probability that the observed peptide matches correspond to a specific protein in the database. Peptide-spectrum match (PSM) denotes the number of spectra that confidently match a given peptide, reflecting the reliability of peptide identification. (**F**) Higher-magnification imaging of MYH9 localization in Sertoli cells. Testes from 17-day-old *Map7*$^{+/-}$ and *Map7*$^{-/-}$ mice were analyzed by immunofluorescence. Cross-sections of seminiferous tubules were stained with antibodies against TUBB3 and MYH9, and with phalloidin to visualize F-actin, together with DAPI to label nuclei. For better visibility, only the grayscale channels of TUBB3, MYH9, and phalloidin for F-actin are shown. Lower-magnification images corresponding to these fields are presented in Supplemental Fig. 5. Scale bar: 10□μm.

**Figure 5. Functional differentiation of Sertoli cells is largely preserved in the absence of**

**MAP7.**

(**A**) UMAP visualization of transcriptomic profiles from Sertoli cells isolated from P19 testes of specified genotypes. The control was prepared by pooling testes from one wild-type and two *Map7*$^{+/-}$ littermate mice. Testes from *Map7*$^{-/-}$ littermates were used for comparison. Clusters were defined based on distinct gene expression patterns. (**B**) Violin plots showing the expression of cluster-specific gene sets, selected from the top 100 differentially expressed genes in each cluster, as identified by Metascape enrichment analysis. (**C**) Control and *Map7*$^{-/-}$ Sertoli cells were visualized separately using UMAPs constructed in Seurat. Using the same datasets, pseudotime trajectories were inferred with Monocle3. For root selection, shared_score (cluster overlap), specificity_score (cluster uniqueness), and entropy_score (transcriptional diversity) were computed, resulting in cluster 1 being selected as the root. The numbers of nodes, edges, branch points, average degree, and diameter of each trajectory are shown below the corresponding UMAPs. (**D**) Parallel comparison of pseudotime distributions between control and *Map7*$^{-/-}$ populations.

**Figure 6. Sertoli apical domain ensures orderly progression of the pachytene stage during meiosis.**

(**A**) Whole-mount immunofluorescence of seminiferous tubules from 8-week-old mice showing GFRα1$^{+}$ spermatogonial stem cells (SSCs). Tubules were stained for GFRα1 and DAPI and imaged from the basal side by z-sectioning. Scale bar, 50 μm. (**B**) Quantification of GFRα1$^{+}$ SSCs per $10^4$ μm$^2$ based on the basal area of seminiferous tubules. Data were collected from 40 tubules per genotype across three independent experiments. (**C**) Immunofluorescence analysis of ZFP541$^{+}$ round spermatids and SYCP3$^{+}$/ZFP541$^{+}$ pachytene spermatocytes in testis sections from 8-week-old mice. Sections were stained with PNA (acrosome marker), SYCP3, ZFP541, and DAPI. Scale bars, 50 and 25 μm. (**D**) Quantification of ZFP541$^{+}$ round spermatids (RS) and SYCP3$^{+}$/ZFP541$^{+}$ pachytene spermatocytes (Pachy Sp) per $10^3$ μm$^2$. Data were obtained from 28 images per genotype across three independent experiments. Statistical significance was assessed by one-way ANOVA ($P$<0.003), followed by the Student's $t$-test, with significance indicated as follows: *, $P<4\times10^{-6}$; **, $P<4\times10^{-5}$. (**E**) UMAP visualization of scRNA-Seq transcriptomic profiles from germ cells isolated from 23-day-old testes from specified genotypes. Clusters were defined based on gene expression patterns. Arrows indicate the direction of germ cell differentiation. Spg, Sp, and RS denote spermatogonia, spermatocytes, and round spermatids, respectively. (**F**) Proportions of indicated germ cell types within each cluster in the indicated mice. To further resolve spermatocyte sub-stages, expression levels of

sex chromosomal genes (bottom panel) were assessed and visualized as violin plots to assist in stage classification. (**G**) Clustered UMAP representations of specified genotypes (left panel). *Prelid1*, a gene expressed through early pachytene (middle panel), and *Ccna1*, a late pachytene-enriched gene (right panel), were used as molecular markers to classify clusters f–j into early, mid, or late pachytene stages.

## References


Adler A, Bangera M, Beugelink JW, Bahri S, van Ingen H, Moores CA, Baldus M. 2024. A structural and dynamic visualization of the interaction between MAP7 and microtubules. *Nat Commun* **15**: 1948.

Bairoch A, Apweiler R. 1999. The SWISS-PROT protein sequence data bank and its supplement TrEMBL in 1999. *Nucleic Acids Res* **27**: 49-54.

Barlan K, Lu W, Gelfand VI. 2013. The microtubule-binding protein ensconsin is an essential cofactor of kinesin-1. *Curr Biol* **23**: 317-322.

Bashamboo A, Ferraz-de-Souza B, Lourenço D, Lin L, Sebire NJ, Montjean D, Bignon-Topalovic J, Mandelbaum J, Siffroi J-P, Christin-Maitre S et al. 2010. Human Male Infertility Associated with Mutations in NR5A1 Encoding Steroidogenic Factor 1. *The American Journal of Human Genetics* **87**: 505-512.

Belevich I, Joensuu M, Kumar D, Vihinen H, Jokitalo E. 2016. Microscopy Image Browser: A Platform for Segmentation and Analysis of Multidimensional Datasets. *PLoS Biol* **14**: e1002340.

Butler A, Hoffman P, Smibert P, Papalexi E, Satija R. 2018. Integrating single-cell transcriptomic data across different conditions, technologies, and species. *Nat Biotechnol* **36**: 411-420.

Byers S, Graham R, Dai HN, Hoxter B. 1991. Development of Sertoli cell junctional specializations and the distribution of the tight-junction-associated protein ZO-1 in the mouse testis. *American Journal of Anatomy* **191**: 35-47.

Cleary JM, Hancock WO. 2021. Molecular mechanisms underlying microtubule growth dynamics. *Curr Biol* **31**: R560-R573.

Du W, Verma A, Ye Q, Du W, Lin S, Yamanaka A, Klein OD, Hu JK. 2024. Myosin II mediates Shh signals to shape dental epithelia via control of cell adhesion and movement. *PLoS Genet* **20**: e1011326.

Dunleavy JEM, O'Bryan MK, Stanton PG, O'Donnell L. 2019. The cytoskeleton in spermatogenesis. *Reproduction (Cambridge, England)* **157**: R53-R72.

Fabre-Jonca N, Allaman JM, Radlgruber G, Meda P, Kiss JZ, French LE, Masson D. 1998. The distribution of murine 115-kDa epithelial microtubule-associated protein (E-MAP-115) during embryogenesis and in adult organs suggests a role in epithelial polarization and differentiation. *Differentiation; research in biological diversity* **63**: 169-180.

Ferlin A, Vinanzi C, Garolla A, Selice R, Zuccarello D, Cazzadore C, Foresta C. 2006. Male infertility and androgen receptor gene mutations: clinical features and identification of

seven novel mutations. *Clinical Endocrinology* **65**: 606-610.

Flanagan JG, Chan DC, Leder P. 1991. Transmembrane form of the kit ligand growth factor is determined by alternative splicing and is missing in the SId mutant. *Cell* **64**: 1025-1035.

Fleming SL, Shank PR, Boekelheide K. 2003a. γ-Tubulin Overexpression in Sertoli Cells In Vivo. II: Retention of Spermatids, Residual Bodies, and Germ Cell Apoptosis1. *Biology of Reproduction* **69**: 322-330.

-. 2003b. γ-Tubulin Overexpression in Sertoli Cells In Vivo: I. Localization to Sites of Spermatid Head Attachment and Alterations in Sertoli Cell Microtubule Distribution1. *Biology of Reproduction* **69**: 310-321.

Grove BD, Vogl AW. 1989. Sertoli cell ectoplasmic specializations: a type of actin-associated adhesion junction? *Journal of Cell Science* **93**: 309-323.

Haque F, Kaku Y, Fujimura S, Ohmori T, Adelstein RS, Nishinakamura R. 2017. Non-muscle myosin II deletion in the developing kidney causes ureter-bladder misconnection and apical extrusion of the nephric duct lineage epithelia. *Developmental Biology* **427**: 121-130.

Heinrich A, Bhandary B, Potter SJ, Ratner N, DeFalco T. 2021. Cdc42 activity in Sertoli cells is essential for maintenance of spermatogenesis. *Cell reports* **37**: 109885.

Heinrich A, Potter SJ, Guo L, Ratner N, DeFalco T. 2020. Distinct Roles for Rac1 in Sertoli Cell Function during Testicular Development and Spermatogenesis. *Cell reports* **31**: 107513.

Hiort O, Holterhus PM, Horter T, Schulze W, Kremke B, Bals-Pratsch M, Sinnecker GH, Kruse K. 2000. Significance of mutations in the androgen receptor gene in males with idiopathic infertility. *The Journal of clinical endocrinology and metabolism* **85**: 2810-2815.

Hofmann MC, McBeath E. 2022. Sertoli Cell-Germ Cell Interactions Within the Niche: Paracrine and Juxtacrine Molecular Communications. *Front Endocrinol (Lausanne)* **13**: 897062.

Hooikaas PJ, Martin M, Mühlethaler T, Kuijntjes GJ, Peeters CAE, Katrukha EA, Ferrari L, Stucchi R, Verhagen DGF, van Riel WE et al. 2019. MAP7 family proteins regulate kinesin-1 recruitment and activation. *J Cell Biol* **218**: 1298-1318.

Ishiguro KI, Matsuura K, Tani N, Takeda N, Usuki S, Yamane M, Sugimoto M, Fujimura S, Hosokawa M, Chuma S et al. 2020. MEIOSIN Directs the Switch from Mitosis to Meiosis in Mammalian Germ Cells. *Dev Cell* **52**: 429-445.e410.

Kikuchi K, Nakamura A, Arata M, Shi D, Nakagawa M, Tanaka T, Uemura T, Fujimori T, Kikuchi A, Uezu A et al. 2018. Map7/7D1 and Dvl form a feedback loop that facilitates

microtubule remodeling and Wnt5a signaling. *EMBO Rep* **19**: e45471.

Kikuchi K, Sakamoto Y, Uezu A, Yamamoto H, Ishiguro KI, Shimamura K, Saito T, Hisanaga SI, Nakanishi H. 2022. Map7D2 and Map7D1 facilitate microtubule stabilization through distinct mechanisms in neuronal cells. *Life science alliance* **5**.

Komada M, McLean DJ, Griswold MD, Russell LD, Soriano P. 2000. E-MAP-115, encoding a microtubule-associated protein, is a retinoic acid-inducible gene required for spermatogenesis. *Genes Dev* **14**: 1332-1342.

La Manno G, Soldatov R, Zeisel A, Braun E, Hochgerner H, Petukhov V, Lidschreiber K, Kastriti ME, Lonnerberg P, Furlan A et al. 2018. RNA velocity of single cells. *Nature* **560**: 494-498.

Luaces JP, Toro-Urrego N, Otero-Losada M, Capani F. 2023. What do we know about blood-testis barrier? current understanding of its structure and physiology. *Front Cell Dev Biol* **11**: 1114769.

Metzger T, Gache V, Xu M, Cadot B, Folker ES, Richardson BE, Gomes ER, Baylies MK. 2012. MAP and kinesin-dependent nuclear positioning is required for skeletal muscle function. *Nature* **484**: 120-124.

Monroy BY, Sawyer DL, Ackermann BE, Borden MM, Tan TC, Ori-McKenney KM. 2018. Competition between microtubule-associated proteins directs motor transport. *Nat Commun* **9**: 1487.

Monroy BY, Tan TC, Oclaman JM, Han JS, Simó S, Niwa S, Nowakowski DW, McKenney RJ, Ori-McKenney KM. 2020. A Combinatorial MAP Code Dictates Polarized Microtubule Transport. *Dev Cell* **53**: 60-72.e64.

Naughton CK, Jain S, Strickland AM, Gupta A, Milbrandt J. 2006. Glial Cell-Line Derived Neurotrophic Factor-Mediated RET Signaling Regulates Spermatogonial Stem Cell Fate1. *Biology of Reproduction* **74**: 314-321.

Nel-Themaat L, Vadakkan TJ, Wang Y, Dickinson ME, Akiyama H, Behringer RR. 2009. Morphometric analysis of testis cord formation in Sox9-EGFP mice. *Dev Dyn* **238**: 1100-1110.

O'Donnell L, Smith LB, Rebourcet D. 2022. Sertoli cells as key drivers of testis function. *Seminars in cell & developmental biology* **121**: 2-9.

Oatley MJ, Racicot KE, Oatley JM. 2011. Sertoli cells dictate spermatogonial stem cell niches in the mouse testis. *Biol Reprod* **84**: 639-645.

Okuda S, Yoshizawa Akiyasu C, Kobayashi D, Takahashi Y, Watanabe Y, Moriya Y, Hatano A, Takami T, Matsumoto M, Araki N et al. 2024. jPOST environment accelerates the reuse

and reanalysis of public proteome mass spectrometry data. *Nucleic Acids Research* **53**: D462-D467.

Pan X, Cao Y, Stucchi R, Hooikaas PJ, Portegies S, Will L, Martin M, Akhmanova A, Harterink M, Hoogenraad CC. 2019. MAP7D2 Localizes to the Proximal Axon and Locally Promotes Kinesin-1-Mediated Cargo Transport into the Axon. *Cell Rep* **26**: 1988-1999.

Roll-Mecak A. 2020. The Tubulin Code in Microtubule Dynamics and Information Encoding. *Dev Cell* **54**: 7-20.

Russell LD, Bartke A, Goh JC. 1989. Postnatal development of the Sertoli cell barrier, tubular lumen, and cytoskeleton of Sertoli and myoid cells in the rat, and their relationship to tubular fluid secretion and flow. *The American journal of anatomy* **184**: 179-189.

Sakuma T, Nakade S, Sakane Y, Suzuki KT, Yamamoto T. 2016. MMEJ-assisted gene knock-in using TALENs and CRISPR-Cas9 with the PITCh systems. *Nature protocols* **11**: 118-133.

Schindelin J, Arganda-Carreras I, Frise E, Kaynig V, Longair M, Pietzsch T, Preibisch S, Rueden C, Saalfeld S, Schmid B et al. 2012. Fiji: an open-source platform for biological-image analysis. *Nat Methods* **9**: 676-682.

Smith LB, Milne L, Nelson N, Eddie S, Brown P, Atanassova N, O'Bryan MK, O'Donnell L, Rhodes D, Wells S et al. 2012. KATNAL1 Regulation of Sertoli Cell Microtubule Dynamics Is Essential for Spermiogenesis and Male Fertility. *PLOS Genetics* **8**: e1002697.

Stuart T, Butler A, Hoffman P, Hafemeister C, Papalexi E, Mauck WM, 3rd, Hao Y, Stoeckius M, Smibert P, Satija R. 2019. Comprehensive Integration of Single-Cell Data. *Cell* **177**: 1888-1902 e1821.

Sung HH, Telley IA, Papadaki P, Ephrussi A, Surrey T, Rørth P. 2008. Drosophila ensconsin promotes productive recruitment of Kinesin-1 to microtubules. *Dev Cell* **15**: 866-876.

Sweeney C, Murphy M, Kubelka M, Ravnik SE, Hawkins CF, Wolgemuth DJ, Carrington M. 1996. A distinct cyclin A is expressed in germ cells in the mouse. *Development* **122**: 53-64.

Takagi I, Yamada K, Sato T, Hanaichi T, Iwamoto T, Jin L. 1990. Penetration and Stainability of Modified Sato's Lead Staining Solution. *Journal of Electron Microscopy* **39**: 67-68.

Tanwar PS, Kaneko-Tarui T, Zhang L, Teixeira JM. 2012. Altered LKB1/AMPK/TSC1/TSC2/mTOR signaling causes disruption of Sertoli cell polarity and spermatogenesis. *Human Molecular Genetics* **21**: 4394-4405.

team P. 2025. RStudio: Integrated Development Environment for R. *Posit Software, PBC,*

*Boston, MA, USA*.

Team RC. 2021. R: A Language and Environment for Statistical Computing. *R Foundation for Statistical Computing, Vienna, Austria*.

Tymanskyj SR, Yang BH, Verhey KJ, Ma L. 2018. MAP7 regulates axon morphogenesis by recruiting kinesin-1 to microtubules and modulating organelle transport. *Elife* **7**: e36374.

Wang F, Zhang Q, Cao J, Huang Q, Zhu X. 2008. The microtubule plus end-binding protein EB1 is involved in Sertoli cell plasticity in testicular seminiferous tubules. *Experimental Cell Research* **314**: 213-226.

Watanabe T, Cheng EC, Zhong M, Lin H. 2015. Retrotransposons and pseudogenes regulate mRNAs and lncRNAs via the piRNA pathway in the germline. *Genome Res* **25**: 368-380.

Willems A, Batlouni SR, Esnal A, Swinnen JV, Saunders PT, Sharpe RM, França LR, De Gendt K, Verhoeven G. 2010. Selective ablation of the androgen receptor in mouse sertoli cells affects sertoli cell maturation, barrier formation and cytoskeletal development. *PLoS One* **5**: e14168.

Xiong Z, Wang C, Wang Z, Dai H, Song Q, Zou Z, Xiao B, Zhao AZ, Bai X, Chen Z. 2018. Raptor directs Sertoli cell cytoskeletal organization and polarity in the mouse testis†. *Biology of Reproduction* **99**: 1289-1302.

Zhou Y, Zhou B, Pache L, Chang M, Khodabakhshi AH, Tanaseichuk O, Benner C, Chanda SK. 2019. Metascape provides a biologist-oriented resource for the analysis of systems-level datasets. *Nat Commun* **10**: 1523.

Kikuchi_Figure 1

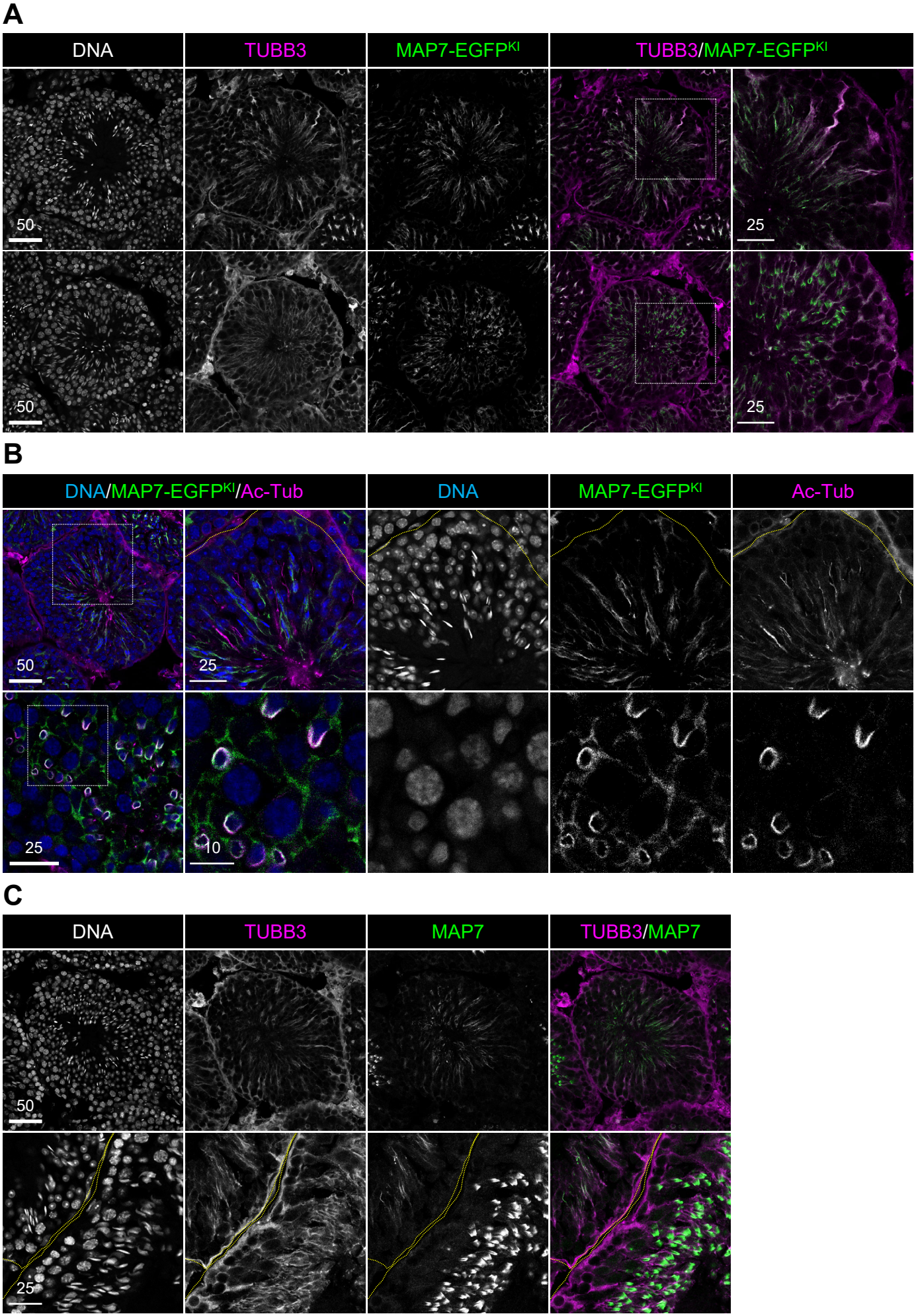

Kikuchi_Figure 2

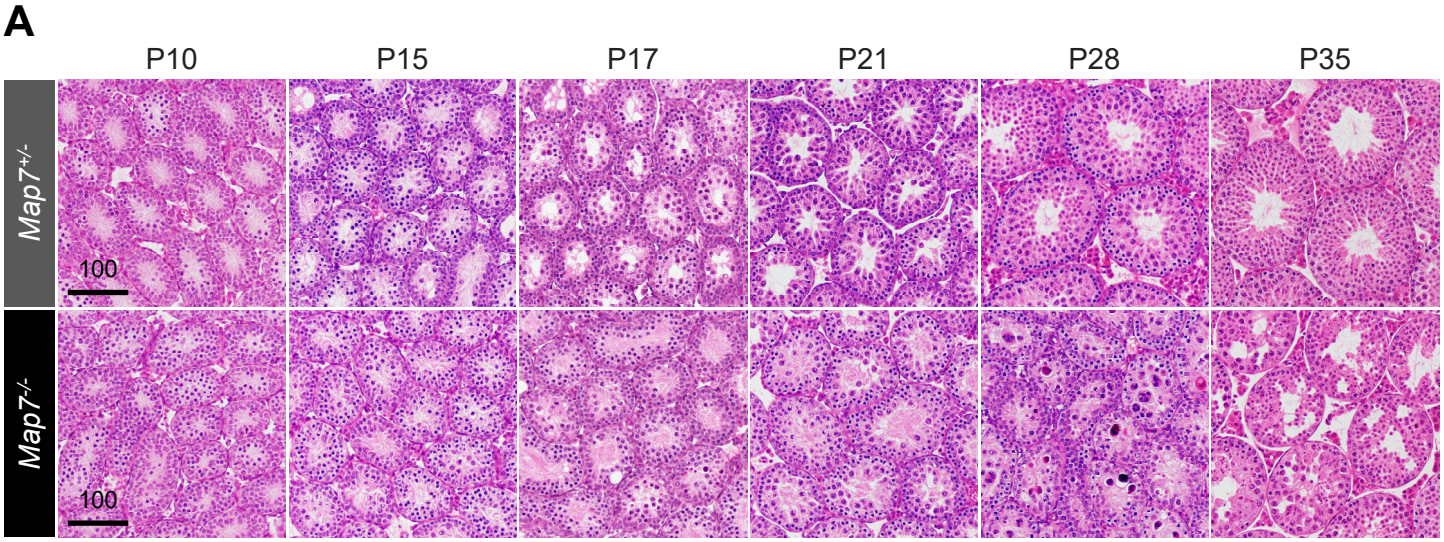


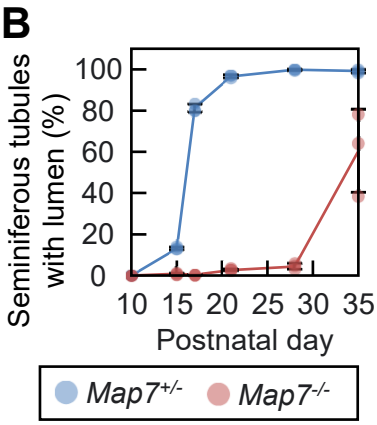


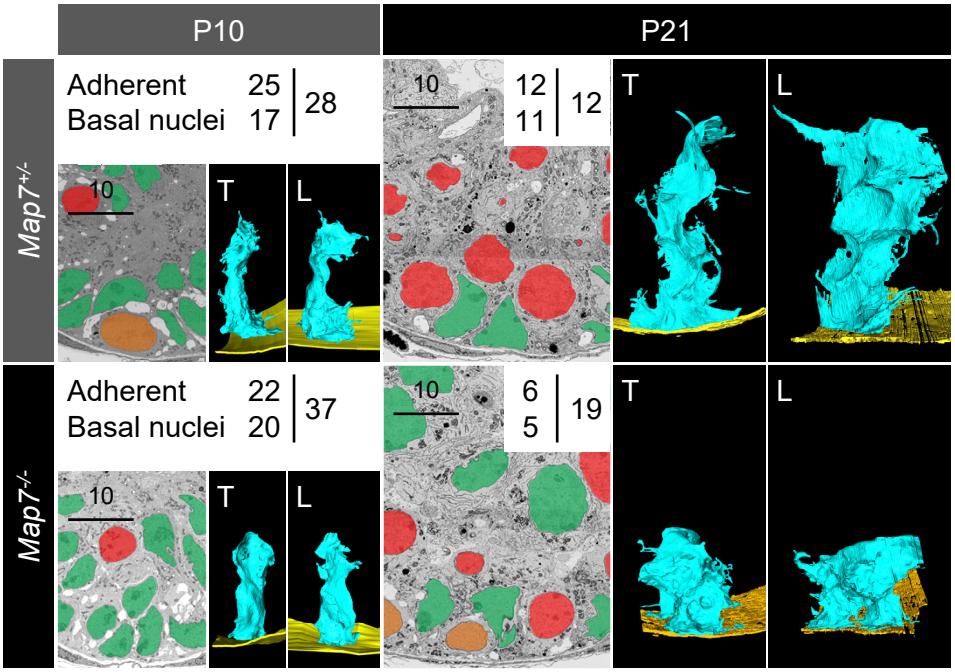


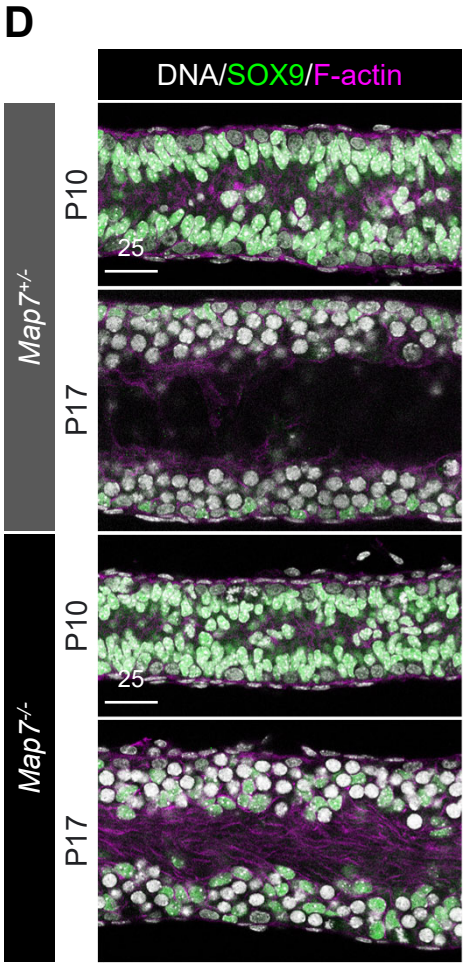


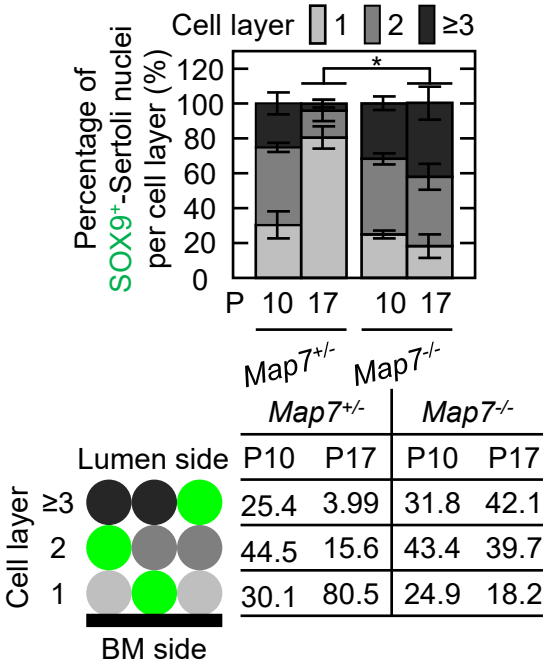


| | Map7+/- | | Map7-/- | |
|---|---|---|---|---|
| | P10 | P17 | P10 | P17 |
| ≥3 | 25.4 | 3.99 | 31.8 | 42.1 |
| 2 | 44.5 | 15.6 | 43.4 | 39.7 |
| 1 | 30.1 | 80.5 | 24.9 | 18.2 |

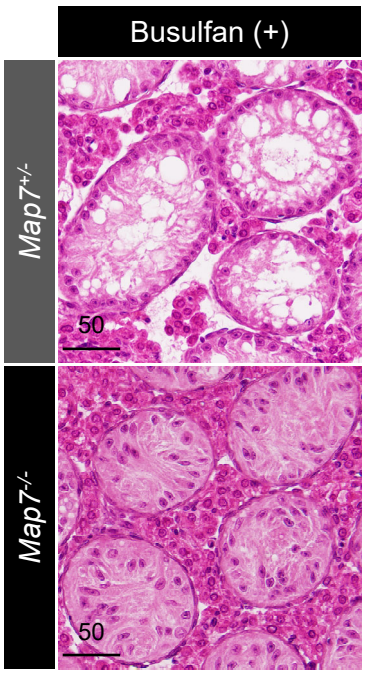

Kikuchi_Figure 3

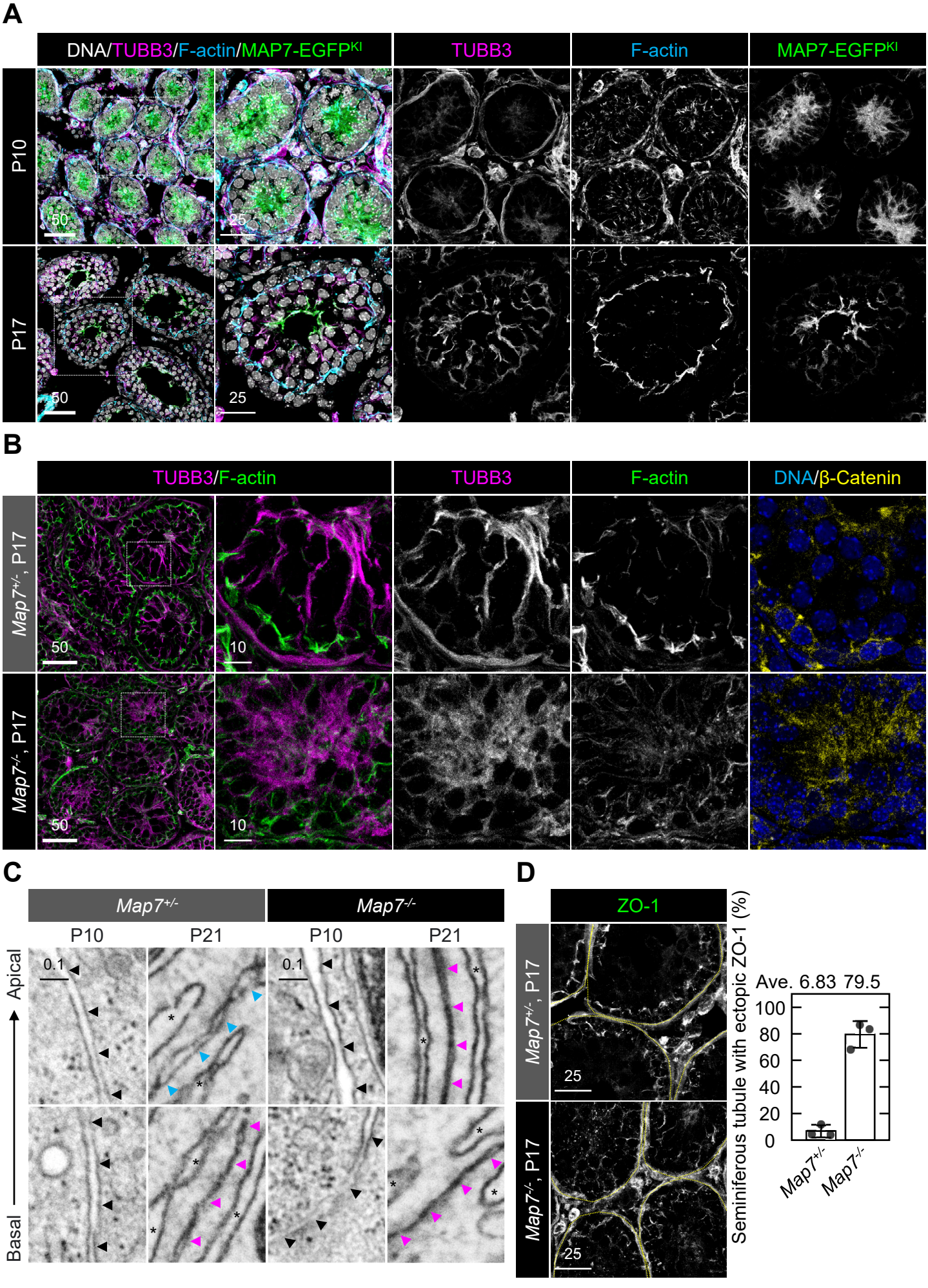

Kikuchi_Figure 4

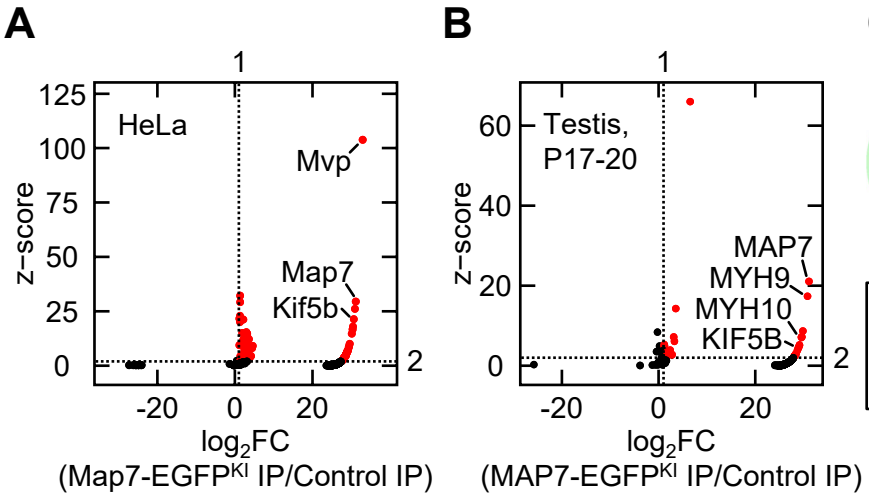


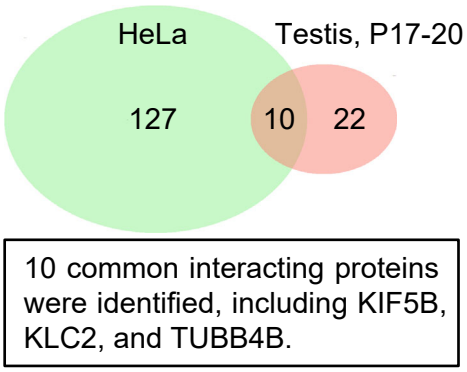


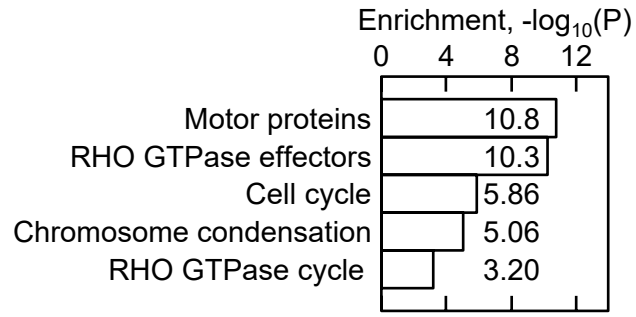


E

| | Name | $log_2FC$ | z-score | Mascot score | PSMs |
|---|---|---|---|---|---|
| MT | MAP7 | 31.08339 | 21.07687 | 2275.273 | 172 |
| MT | KIF5B | 28.90763 | 4.437005 | 503.575 | 24 |
| MT | TUBB3 | 28.41413 | 3.06684 | 357.6893 | 18 |
| MT | KLC2 | 28.0491 | 2.315854 | 277.7294 | 16 |
| AF | MYH9 | 30.8082 | 17.36587 | 1880.151 | 90 |
| AF | ACTC1 | 29.83043 | 8.673716 | 954.6707 | 43 |
| AF | MYH10 | 29.5447 | 7.062721 | 783.1432 | 44 |
| IF | VIM | 28.92826 | 4.505102 | 510.8255 | 24 |

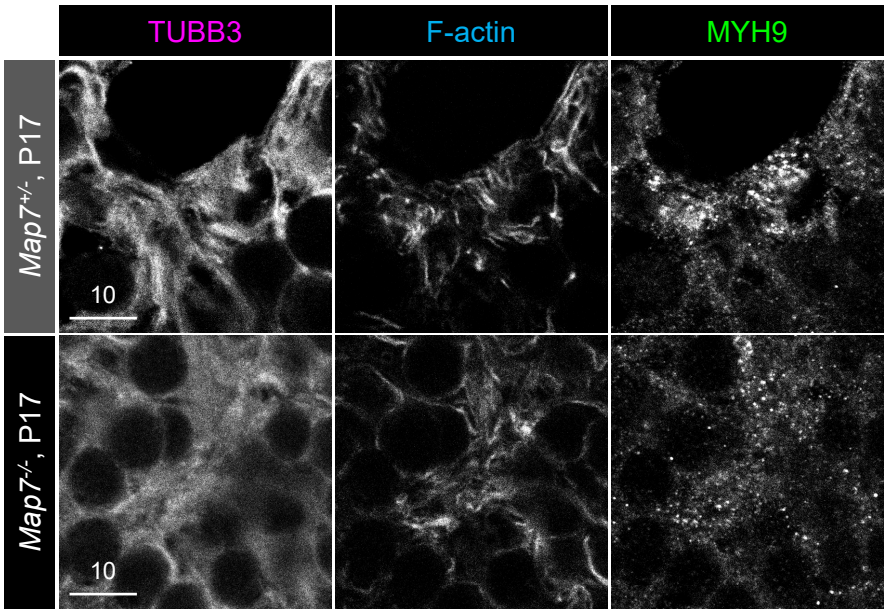

Kikuchi_Figure 5

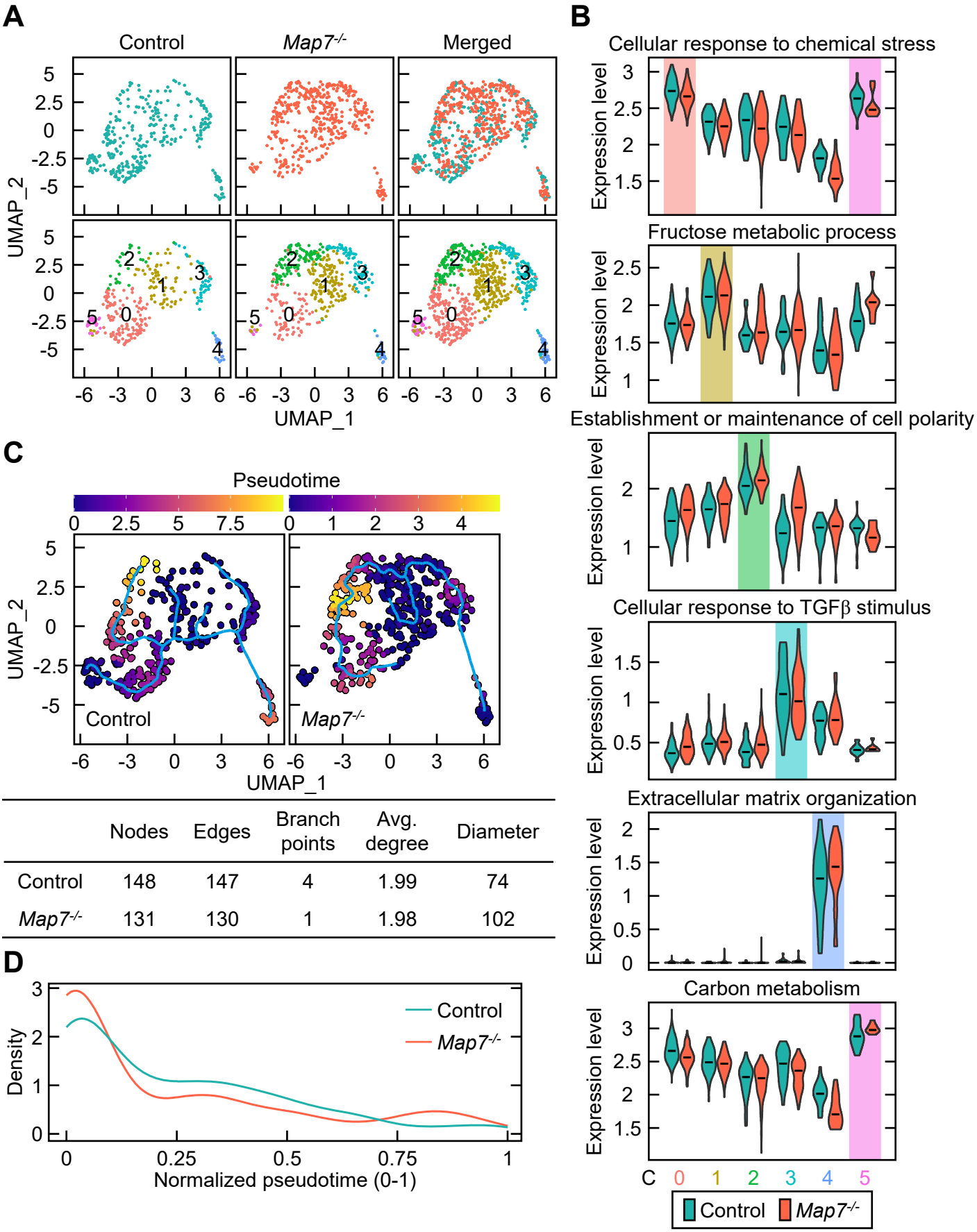


| | Nodes | Edges | Branch points | Avg. degree | Diameter |
|---|---|---|---|---|---|
| Control | 148 | 147 | 4 | 1.99 | 74 |
| *Map7*$^{-/-}$ | 131 | 130 | 1 | 1.98 | 102 |
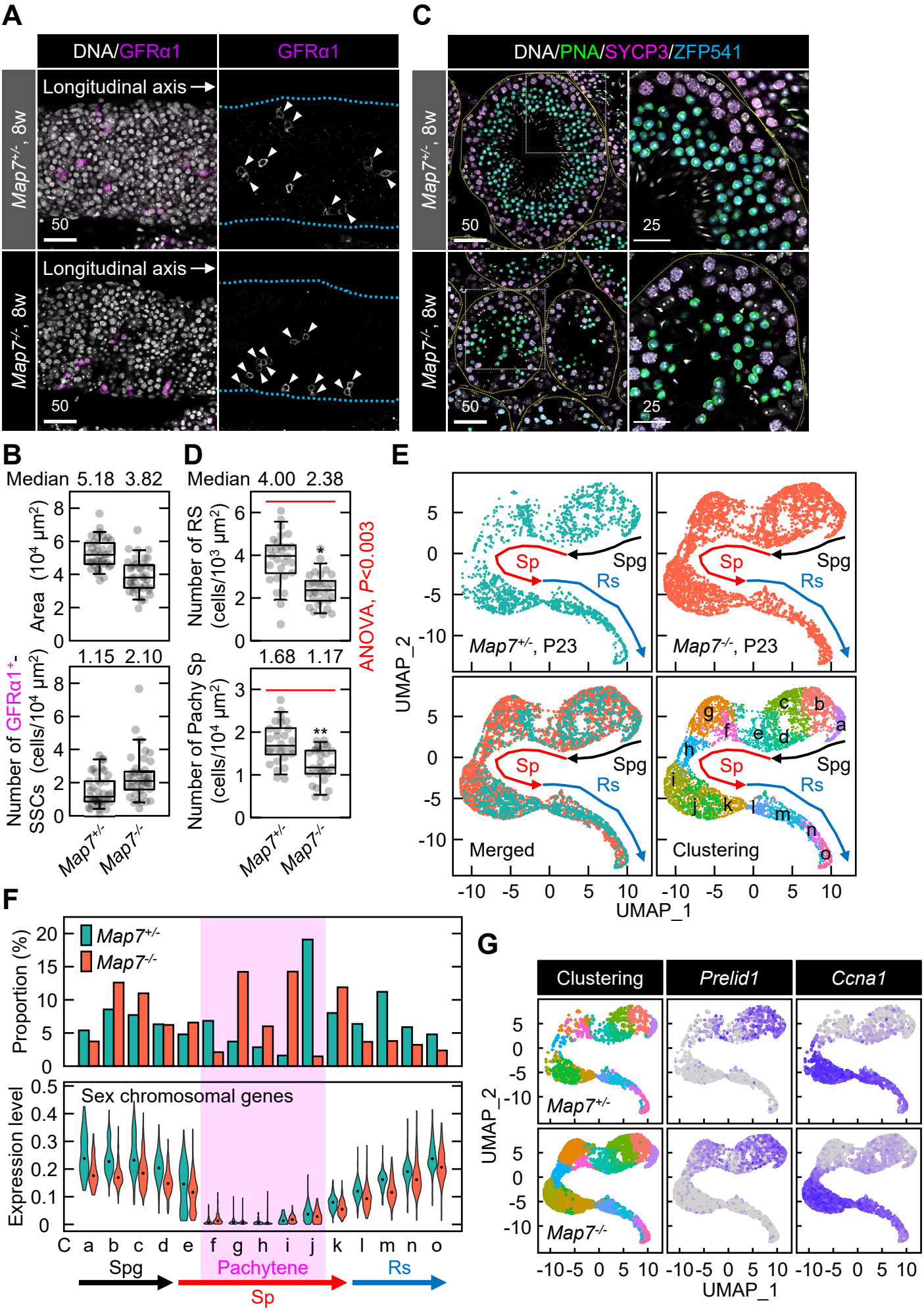
Kikuchi_Figure 6